Research Square

Preprints are preliminary reports that have not undergone peer review.
They should not be considered conclusive, used to inform clinical practice,
or referenced by the media as validated information.

Numerical Optimization of Electron Transport Layer-Free Perovskite Solar Cells Utilizing Titanium-based Perovskite Absorber with Feasibility for Low-Cost Carbon Back-Contact

Iorhom A. Tyom
Joseph Sarwuan Tarka University Makurdi (Federal University of Agriculture Makurdi)
Peverga R. Jubu
peverga.jubu@uam.edu.ng
Joseph Sarwuan Tarka University Makurdi (Federal University of Agriculture Makurdi)
Victor M. Igba
Baba Ahmed University
Otor D. Abi
Joseph Sarwuan Tarka University Makurdi
A. Nathan-Abutu
Joseph Sarwuan Tarka University Makurdi (Federal University of Agriculture Makurdi)
O. M. Enefola
Joseph Sarwuan Tarka University Makurdi (Federal University of Agriculture Makurdi)
Michael B. Ochang
Joseph Sarwuan Tarka University Makurdi (Federal University of Agriculture Makurdi)
Francis Aungwa
Joseph Sarwuan Tarka University Makurdi (Federal University of Agriculture Makurdi)
Ketonze V. Ketu
The University of Bamenda
Dehiin D. Hile
Joseph Sarwuan Tarka University Makurdi (Federal University of Agriculture Makurdi)
Julius N. Tsaviv
Joseph Sarwuan Tarka University Makurdi

Research Article

Keywords: Perovskite solar cells, Cs2TiBr6 perovskite, Carbon back contact, Electron transport layer-free, SCAPS-1D simulation

Posted Date: September 23rd, 2026

DOI: https://doi.org/10.21203/rs.3.rs-10752527/v1

License: This work is licensed under a Creative Commons Attribution 4.0 International License.
Read Full License

Additional Declarations: No competing interests reported.

Numerical Optimization of Electron Transport Layer-Free Perovskite Solar Cells Utilizing Titanium-based Perovskite Absorber with Feasibility for Low-Cost Carbon Back-Contact

Iorhom A. Tyom [a], Peverga R. Jubu [a *], Victor M. Igba [a, b], Otor D. Abi [c], A. Nathan-Abutu [a], O. M. Enefola [a], Michael B. Ochang [a], Francis Aungwa [a], Ketonze V. Ketu [d], Dehiin D. Hile [a, e], Julius N. Tsaviv [f]

[a] Department of Industrial Physics, Joseph Sarwuan Tarka University Makurdi (Federal University of Agriculture Makurdi) P.M.B. 2373, Makurdi, Benue State, Nigeria.

[b] Department of software engineering, Baba-Ahmed University, Kano

[c] Department of Physics, Joseph Sarwuan Tarka University Makurdi P.M.B. 2373, Makurdi, Benue State, Nigeria.

[d] Department of Biochemistry, Faculty of Science, The University of Bamenda, Cameroon

[e] Department of Physics, University of Zululand, Kwadlangezwa. 3886, South Africa

[f] Department of Physics, Joseph Sarwuan Tarka University Makurdi P.M.B. 2373, Makurdi, Benue State, Nigeria.

Corresponding author: peverga.jubu@uam.edu.ng (**P. R. Jubu**)

Abstract

Electron-transport-layer-free (ETL-free) perovskite solar cells (PSCs) offer a route to simpler and potentially lower-cost photovoltaics. However, high-performance lead-free Cs_2TiBr_6 devices remain limited by interfacial recombination, inefficient charge extraction, and dependence on expensive noble-metal contacts. Moreover, the combined use of a $CuSbS_2$/CuI bilayer hole-transport layer with low-cost carbon back-contact engineering has not been systematically explored for ETL-free Cs_2TiBr_6 cells. Herein, SCAPS-1D was deployed to design and optimize FTO/Cs_2TiBr_6/$CuSbS_2$/CuI PSCs by examining layer thicknesses, carrier concentrations, bulk and interface defect densities, electron capture cross-section, series and shunt resistances, temperature, and illumination intensity. The $CuSbS_2$/CuI bilayer prototype outperformed the corresponding single-HTL architectures, providing a PCE of 11.84%. Sensitivity analysis identified Cs_2TiBr_6 bulk defect density as the dominant parameter, followed by shunt resistance, $CuSbS_2$ acceptor concentration, and Cs_2TiBr_6/$CuSbS_2$ interface quality. After simultaneous optimization, the Au-contact device achieved V_{OC}, J_{SC}, FF, and PCE of 1.26 V, 23.57 mA/cm^2, 89.12%, and 26.49%, respectively. Remarkably, replacing Au with carbon preserved the same 26.49% PCE with an essentially unchanged FF of 89.11%, showcasing the electronic feasibility of a low-cost rear

electrode. Both contacts also demonstrated matched temperature- and concentration-dependent behavior. These findings establish a competitive ETL-free Cs_2TiBr_6 architecture in which bilayer hole-selective engineering enables high simulated PCE while supporting carbon-contact substitution for simplified, scalable, and economically attractive lead-free photovoltaics. The simulated outcomes are subject to simplified one-dimensional modeling assumptions. Therefore, experimental verification of absorber quality, interface passivation, carbon-electrode resistance, microstructure, and long-term operational stability is required during practical device fabrication.

Keywords: Perovskite solar cells; Cs_2TiBr_6 perovskite; Carbon back contact; Electron transport layer-free; SCAPS-1D simulation

1. Introduction

The increasing global need for clean, sustainable, and affordable energy has accelerated efforts to develop renewable technologies that can decrease dependence on fossil fuels and mitigate greenhouse gas emissions. Among the existing renewable energy options, solar photovoltaic (PV) technology has become one of the most attractive because sunlight is widely available, PV systems are environmentally friendly and readily scalable, and production costs have continued to decline [1, 2]. Over the past decade, perovskite solar cells (PSCs) have become a prominent focus of photovoltaic research because of their favourable optoelectronic properties, including high light absorption, long carrier diffusion lengths, adjustable bandgaps, weak exciton binding energies, and compatibility with low-temperature-solution processing. Since the early work of Kojima et al. in 2009, who reported a power conversion efficiency (PCE) of 3.8% using organometal halide perovskites, PSC performance has improved rapidly. According to the latest National Renewable Energy Laboratory (NREL) efficiency chart, certified single-junction PSCs now exceed 27%, while perovskite/silicon tandem devices have surpassed 34%, placing PSCs among the most competitive photovoltaic technologies currently available [3-5]. Despite this progress, large-scale commercialization remains limited by the toxicity and environmental concerns linked to Pb-containing absorbers, which has encouraged intensive research into stable and environmentally safer lead-free alternatives. Only recently, Xu et al. have reported a high PCE of 24.2% and V_{OC}

of 54.2 V performance for scalable (module level), industrially viable perovskite photovoltaics, using $Cs_{0.03}FA_{0.97}PbI_3$ perovskite absorber [6].

Among the different lead-free perovskite materials, vacancy-ordered double perovskites with the general formula Cs_2TiX_6 (X = Cl, Br, or I) have attracted growing interest because of their chemical stability, low toxicity, and use of earth-abundant constituent elements. Specifically, Cs_2TiBr_6 possesses a reliable bandgap of about 1.8 eV, robust thermal and moisture stability, high visible light absorption, high resistance to structural degradation, making it an attractive absorber for emerging photovoltaic technologies [7-9]. Nevertheless, practical device performance is still limited by relatively low carrier mobility, pronounce excitonic effects, native defect states, and non-radiative carrier recombination losses, all of which impede charge collection and limit photovoltaic efficiency [9, 10]. To mitigate these channelings, recent studies have focused on interface modification, defect-state suppression, transport-layer optimization, and electrode design. Numerical investigations have shown that careful control of transport layers, interface defect density, absorber thickness, and carrier concentration can substantially improve the performance of Cs_2TiBr_6-based PSCs [11-13]. For example, Mercy and Wilson reported a simulated PCE of 23.77% for FTO/CdS/Cs_2TiBr_6/Cu_2SbS_2/Au [11], Gupta et al. predicted 34.24% using FTO/SnO_2/Cs_2TiBr_6/CBTS/Au [12], while Lin et al. proposed the double hole-transport-layer (HTL) structure FTO/CeO_x/Cs_2TiBr_6/CZTS/P_3HT/Au with a simulated efficiency above 22% [9]. Other numerical studies using CuI-, CNTS-, $MASnBr_3$-, and MoO_x-based HTLs have also highlighted the importance of interface quality and suitable energy-band alignment in achieving high device performance [9, 11, 12, 14-17].

More recently ETL-free PSCs have gained attention as a practical route to reducing device complexity, fabrication cost, and processing temperature while limiting parasitic optical absorption and recombination losses introduced by additional heterointerfaces [18-21]. Removing the ETL also simplifies large-scale manufacturing and supports the development of all-inorganic photovoltaic structures with improved long-term stability. Although ETL-free PSCs have been widely studied for Pb-based absorbers [20, 22-24]. PCEs of 16.47% [23], 22.47% [22], and 23.04% [20] have been recorded from experimental Pb-based PSCs. Comparatively few investigations have considered either ETL- or HTL-free Cs_2TiBr_6 devices. Sen et al. [25] experimentally investigated a transport materials-free FTO/Cs_2TiBr_6/Ag PSC using graphene quantum dots and

obtained a low PCE of 1.02%. You et al. [14] simulated FTO/Cs_2TiBr_6/$MASnBr_3$/Au and received a PCE of 19.63%. Jubu et al. [26] simulated FTO/Cs_2TiBr_6/CZTS/NiO/Au and achieved a PCE of 27.78%. Also, Jubu and co-worker obtained a PCE of 27.14% using FTO/Cs_2TiBr_6/CZTSe/CuO/Pt architecture. In a related study, Jubu et al. [27] reported a higher a high PCE of 30.75% for an ETL-HTL-assisted FTO/CeO_x/Cs_2TiBr_6/Cu_2O/CuO/Pt design [27]. Some of the architectures proposed by Jubu et al [26, 27] achieved PCEs above the Shockley-Queisser limit of 26.86% for an absorber of bandgap of 1.8 eV [28]. This is because those devices incorporate an HTL (CZTSe, or CuO with a lower bandgap), which also served as a secondary absorber layer and extended the light absorption into longer wavelength to support career generation.

Further still, Karmaker et al. [15] proposed an Cs_2TiBr_6-based PSC design Pt/$CuSbS_2$/Cs_2TiBr_6/ZnO/FTO that attained a PCE of 26.96%. So far, however, the studies on Cs_2TiBr_6 based PSCs have employed high-cost metal back contacts (Pt and Au). These high work function metals are employed as rear contacts because their work functions align well with the valence-band/HTL energy levels, which reduce the hole-extraction barrier and promote a more ohmic contact. This boosts hole collection, suppresses interfacial recombination, and can increase open circuit voltage (V_{OC}), fill factor (FF), and PCE [29, 30]. Particularly, a high work function rear contact is employed on a Cs_2TiBr_6 PSC because it has relatively deep valence-band energetics and moderately n-type character, which can create a substantial barrier for hole extraction at a low-work-function metal contact [31]. Its larger bandgap of 1.8 eV is relatively favourable for high photovoltaic performance because of its tendency to not utilize a substantial portion of the solar spectrum to generate more carrier. To overcome these drawbacks therefore, high work function is employed to minimize the hole-extraction barrier, improve energy-level alignment, and suppress interfacial recombination, thereby achieving higher boosting device performance. Nevertheless, these expensive precious metals (Pt and Au) can increase the fabrication cost and limit the scalability of Cs_2TiBr_6 for commercialization. Therefore, the deployment of low-cost rear contact on an ETL-free configuration is essential for a simpler design to ensure large-scale production.

Carbon electrodes have recently attracted increasing interest as inexpensive, earth-abundant, chemically inert, and scalable alternatives. Carbon can be deposited using simple, vacuum-free fabrication techniques while providing excellent operational stability. It can also be applied by the simple and low-cost doctor-blade method [8, 32]. The selection of suitable HTLs

for the design of an Cs_2TiBr_6-based PSC that can perform optimally while employing a relatively low work function and cost-effective carbon contact is critical for scalability, especially in a simpler ETL-free architecture. The selection of $CuSbS_2$/CuI bilayer can enable high device efficiency by combining favorable hole extraction at the Cs_2TiBr_6/$CuSbS_2$ interface with strong electron blocking and rapid hole transport through CuI. Consequently, the carbon electrode would mainly serve as an efficient hole collector, minimizing the performance penalty associated with replacing Au and Pt.

The present work proposes and numerically investigates a novel ETL-free lead-free PSC employing the architecture FTO/Cs_2TiBr_6/$CuSbS_2$/CuI/Au. To the best of our knowledge, no previous study has systematically investigated the combined use of a $CuSbS_2$/CuI double HTL together with Au or carbon back-contact engineering in an ETL-free Cs_2TiBr_6 solar cell. Using SCAPS-1D software, the effects of film thickness, carrier concentrations, bulk and interface defect densities, electron capture cross-section, and back contact engineering are comprehensively optimized. The investigations arrived at a high-performance optimized devices utilizing Au and carbon back contacts (FTO/Cs_2TiBr_6/$CuSbS_2$/CuI/C and FTO/Cs_2TiBr_6/$CuSbS_2$/CuI/C). Interestingly, both the optimized Au- and C-back-contact-based configurations attains equivalent value of PCE. Interestingly, the optimized PCEs are equivalent to the Shockley-Queisser limit of 26.86% predicted for an absorber with a bandgap of 1.8 eV, indicating that the proposed device architectures operate near its theoretical efficiency limit. Finally, the optimized Au and C-contact devices are evaluated under varying operating temperatures and solar concentrations to assess their suitability for efficient and stable ETL-free Cs_2TiBr_6-based PSCs. It is hoped that this study would extend the literature for Cs_2TiBr_6-based PSCs towards scalability.

2. Numerical Simulation of the PSCs

Several software packages are available for solar cell simulations, including SCAPS-1D, AMPS, PC1D, AFORS-HET, Silvaco Atlas, and Comsol Multiphysics. Among these, SCAPS-1D is particularly preferred because it can simulate device performance under both illuminated and dark conditions. It offers a simple interface, models heterojunctions with up to seven layers, eliminates the need for standard C-f and C-V measurements, and provides reliable quantum efficiency (QE)

spectra. Most importantly, it is a non-commercial software unlike the others. Through the SCAPS-1D program, solar cell properties like current density-voltage (J-V) characteristics, band structure, carrier concentrations, electric potential, and recombination behaviour can be investigated. The program achieves this by numerically solving the fundamental semiconductor equations using user-supplied parameters. Accurate input data and moderate values of parameters are essential for the simulated device to closely represent real systems. The tool is based on solving Poisson's equation (Eq. 1) together with electron (Eq. 2) and hole (Eq. 3) continuity equations, which collectively describe the relationship between charge carriers, electrostatic potential, impurity doping, recombination (R)-generation (G) rates, and current densities of electrons (J_n) and holes (J_p).

Solution to the drift-diffusion model provides the transport properties of electrons and holes, according Eqs. (4) and (5).

$$\frac{d^2}{dx^2}\psi(x) = \frac{q}{\varepsilon_0 \varepsilon_r}\left[p(x) - n(x) + N_D^+(x) - N_A^-(x) + \rho_p - \rho_n\right] \quad (1)$$

$$\frac{\partial n}{\partial t} = \frac{1}{q}\frac{\partial J_n}{\partial x} + (G_n - R_n) \quad (2)$$

$$\frac{\partial p}{\partial t} = \frac{1}{q}\frac{\partial J_p}{\partial x} + \left(G_p - R_p\right) \quad (3)$$

$$J_n = q\mu_n n\varepsilon + qD_n \partial n \quad (4)$$

$$J_p = q\mu_p p\varepsilon + qD_p \partial p \quad (5)$$

where the electrostatic potential is represented by ψ, while the electron and hole concentrations are expressed as $n(x)$ and $p(x)$, respectively. The parameters ε_r and ε_0 denote the relative and vacuum permittivity, and N_D and N_A signify donor and acceptor doping levels. The distributions of holes and electrons are given by ρ_p and ρ_n, with q symbolizing the elementary charge. The n and p indicate electron and hole densities. The μ_n and μ_p represent *e* and *h* mobilities, whereas D_n and D_p are the are the diffusion coefficients. The diffusion coefficients are governed by carrier mobility and are also affected by the carrier lifetime.

It should be emphasized that electron and hole recombination arises from both radiative processes and deep-level traps. The latter is governed by the Shockley–Read–Hall (SRH) mechanism, where the recombination rate, expressed in Eq. 6, is determined by the minority carrier lifetime (τ) and the defect density as described in Eq. 7.

$$R_{SRH} = \frac{(np - n_i^2)}{\tau\left[p + n + n_i \exp\left(\frac{E_i - E_t}{k_B T}\right) + n_i \exp\left(\frac{E_i - E_t}{k_B T}\right)\right]} \quad (6)$$

$$\tau = (\sigma N_t v_{th})^{-1} \quad (7)$$

where σ is the capture-cross-section for either e or h, v_{th} represents thermal velocity, E_i represents the intrinsic energy level, and E_t is the energy level of the trap.

Table 1. SCAPS-1D Simulation parameters for the various PSCs

Parameter	Layer			
	FTO	Cs_2TiBr_6	$CuSbS_2$	CuI
	[9]	[9]	[11, 33]	[34, 35]
Thickness (μm)	0.5	0.5	0.1	0.2
E_g (eV)	3.5	1.8	1.58	3.1
χ (eV)	4.3	4.47	4.2	2.1
ε_r	9.0	10	14.6	6.5
N_C (cm^{-3})	2.2×10^{18}	6.0×10^{19}	2×10^{18}	2.5×10^{20}
N_V (cm^{-3})	1.8×10^{19}	2.0×10^{19}	1×10^{19}	2.5×10^{20}
μ_n ($cm^2V^{-1}\ s^{-1}$)	200	4.4	49	44
μ_p ($cm^2V^{-1}\ s^{-1}$)	10	2.5	49	44
e V_{th} (cm/s)	1×10^7	1×10^7	1×10^7	1×10^7
h V_{th} (cm/s)	1×10^7	1×10^7	1×10^7	1×10^7
N_D (cm^{-3})	0	1×10^{13}	0	0

N_A (cm^{-3})	2×10^{19}	1×10^{13}	1×10^{16}	1×10^{16}
N_t (cm^{-3})	1×10^{15}	1×10^{14}	1×10^{15}	1×10^{14}
Capture cross section for electrons (cm^2)	1×10^{-15}	1×10^{-15}	1×10^{-15}	1×10^{-15}
Capture cross section for electrons (cm^2)	1×10^{-15}	1×10^{-15}	1×10^{-15}	1×10^{-15}

Table 2**.** Interface defect parameters [33, 36]

Parameters	Cs_2TiBr_6/ $CuSbS_2$	$CuSbS_2$/CuI
Capture cross section for electrons (cm^2)	1×10^{-19}	1×10^{-19}
Capture cross section for holes (cm^2)	1×10^{-19}	1×10^{-19}
Energetic distribution	Single	Single
Energy level with respect to E_v (eV)	0.60	0.60
Characteristic energy (eV)	0.10	0.10
Interface defect density (cm^{-2})	1×10^{13}	1×10^{10}

2.1 Solar cell Structure

Fig, 1 depicts the PSC architectures: FTO/Cs_2TiBr_6/CuI/Au and FTO/Cs_2TiBr_6/$CuSbS_2$/Au (Fig. 1a), and FTO/Cs_2TiBr_6/$CuSbS_2$/CuI/Au, (Fig. 1b). The FTO is utilized as the front contact, Cs_2TiBr_6 is the absorber layer, $CuSbS_2$ and CuI are the HTLs, and gold (Au) is the back contact. The work function of the Au and FTO are 5.1 and 4.4 eV, respectively [33, 37] . The three prototype solar cells are simulated to selected the device with best performance metric for further optimization. Fig. 1c illustrates the energy-band profile. The simulation was done under AM 1.5G light source with power density of 100 mW/cm^2, a working frequency of 1×10^6 Hz, scanning voltage range of 0-1.5 V, and a working temperature of 300 K [33, 37]. Table 1 summarizes the data utilized for each layer. Table 2 displays the various interface properties.

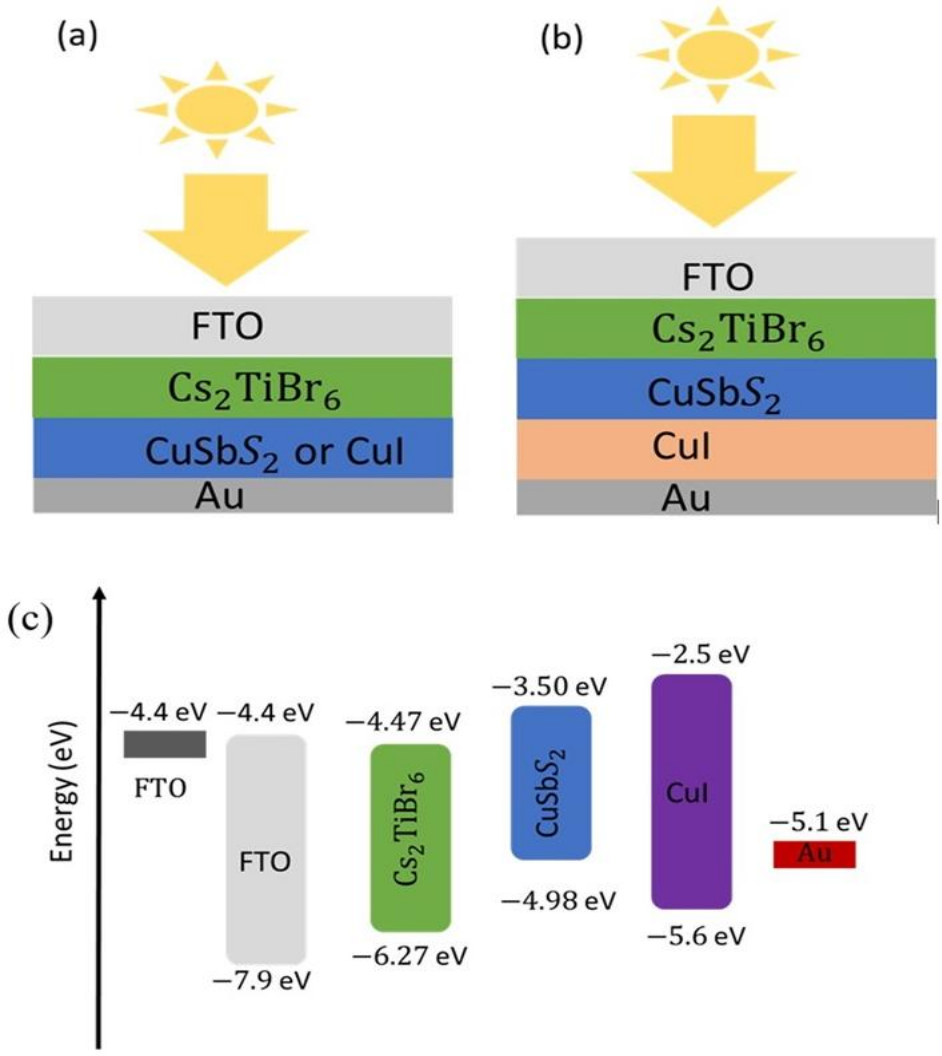


Figure 1. (a) Schematic of the PSC utilizing single HTL, (b) Schematic of the PSC utilizing double HTL, (c) Energy level diagram of the PSC various layers.

3. Results and Discussion

3.1 Photovoltaic performance of the prototype PSCs

The photovoltaic performance of the three prototype ETL-free PSCs strongly depends on the hole transport layer (HTL) configuration, as summarized in Table 3. Among the investigated

architectures, the FTO/Cs_2TiBr_6/$CuSbS_2$/CuI/Au device with a double HTL exhibited the best performance, achieving V_{OC}, J_{SC}, FF, and PCE of 0.80 V, 19.03 mA/cm^2, 77.67%, and 11.84%, respectively. In comparison, the single-HTL devices (FTO/Cs_2TiBr_6/$CuSbS_2$/Au and FTO/Cs_2TiBr_6/CuI/Au yielded considerably lower efficiencies of 8.36% and 4.26%, respectively. These results demonstrate that the simultaneous incorporation of $CuSbS_2$ and CuI produces a pronounced synergistic improvement in charge extraction and recombination suppression.

The $CuSbS_2$-based device exhibited superior performance to the CuI-based counterpart because $CuSbS_2$ exhibits a narrower bandgap (1.58 eV) and greater electron affinity (4.2 eV), resulting in a more favorable energy-level alignment with Cs_2TiBr_6. The relatively small valence-band offset (VBO) of +0.49 eV facilitated efficient hole extraction while the positive conduction-band offset (CBO) of +0.27 eV suppressed electron leakage from reaching the rear contact (Fig. 3a). As a result, electron-hole recombination at the absorber/HTL interface was reduced, leading to higher J_{SC}, FF, and PCE. Although CuI demonstrate high hole mobility and a wide optical bandgap, its large VBO (+1.07 eV) with Cs_2TiBr_6 introduced a significant energetic barrier for hole transfer (Fig. 3b). This barrier hindered hole extraction, promoted carrier accumulation at the interface, and enhanced Shockley-Read-Hall recombination. The resulting increase in recombination losses remarkably suppressed photocurrent generation and photovoltaic performance, explaining the poor PCE of the CuI-based device.

The enhanced photovoltaic performance of the $CuSbS_2$/CuI based device arose from complementary electronic functions provided by the two HTLs. $CuSbS_2$ offered favorable band alignment that enabled effective hole transfer while suppressing electron backflow. The outer CuI layer, possessing a wide bandgap and strong hole-transfer capability, improved hole transport toward the Au electrode, enhanced back-contact selectivity, and further suppressed electron leakage. The stepwise valence-band alignment established by the $CuSbS_2$/CuI bilayer (Fig. 3c) reduced interfacial band discontinuities, strengthened the built-in electric field near the back contact, and promoted selective charge transport. Simultaneously, the dual HTL decreased interfacial recombination by promoting charge separation and enhanced quasi-Fermi-level splitting under illumination. The simultaneous improvement in V_{OC}, J_{SC}, and FF observed for the bilayer device confirm that photovoltaic performance is controlled not only by the intrinsic properties of the Cs_2TiBr_6 absorber but also by optimized interfacial design and carrier-selective

contacts. The $CuSbS_2$/CuI double-HTL architecture therefore provides a favourable combination of efficient hole extraction, excellent electron blocking, reduced recombination, and improved carrier collection. These makes it the preferred prototype for subsequent device optimization.

The quantum efficiency (QE) spectra show that the $CuSbS_2$/CuI double-HTL PSC has the highest light harvesting capability and carrier-generation efficiency over most of the visible region. This is consistent with its superior J_{SC} and PCE exhibited this architecture (Table 3). In contrast, the CuI-only device shows the poorest QE because its large valence-band offset with Cs_2TiBr_6 hinders hole extraction and increases carrier accumulation and recombination. Also, the larger bandgap of CuI limit is light absorption range, and hence lower carrier generation.

Table 3. Comparison of PV performance of the prototype cells

Solar cell	V_{OC} (V)	J_{SC} (mA/cm^2)	FF (%)	PCE (%)
FTO/Cs_2TiBr_6/$CuSbS_2$/CuI/Au	0.80	19.03	77.67	11.84
FTO/Cs_2TiBr_6/$CuSbS_2$/Au	0.68	17.80	68.96	8.36
FTO/Cs_2TiBr_6/CuI/Au	0.43	16.50	60.04	4.26

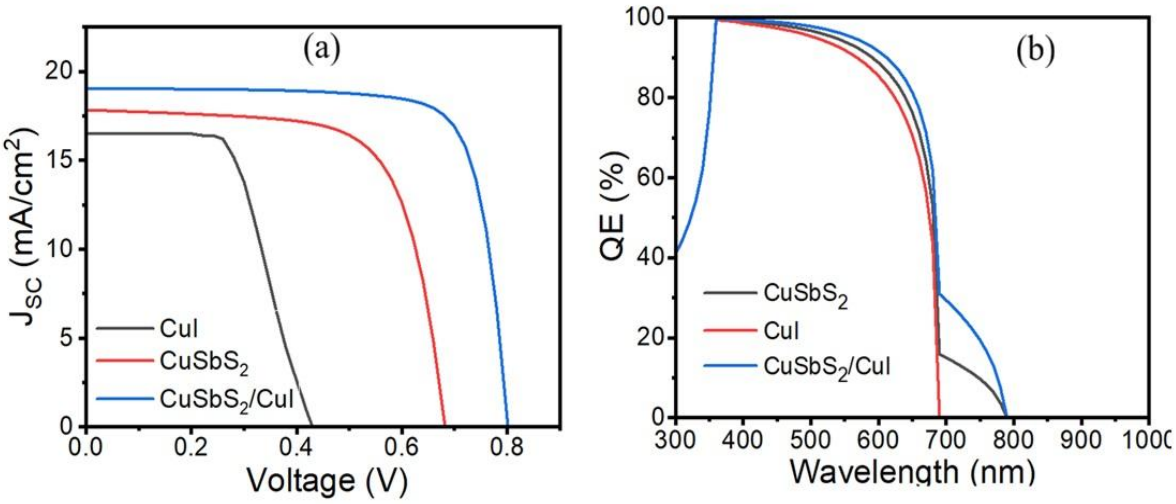


Figure 2. (a) J-V curves for the prototype PSCs, (b) Wavelength-dependent QE.

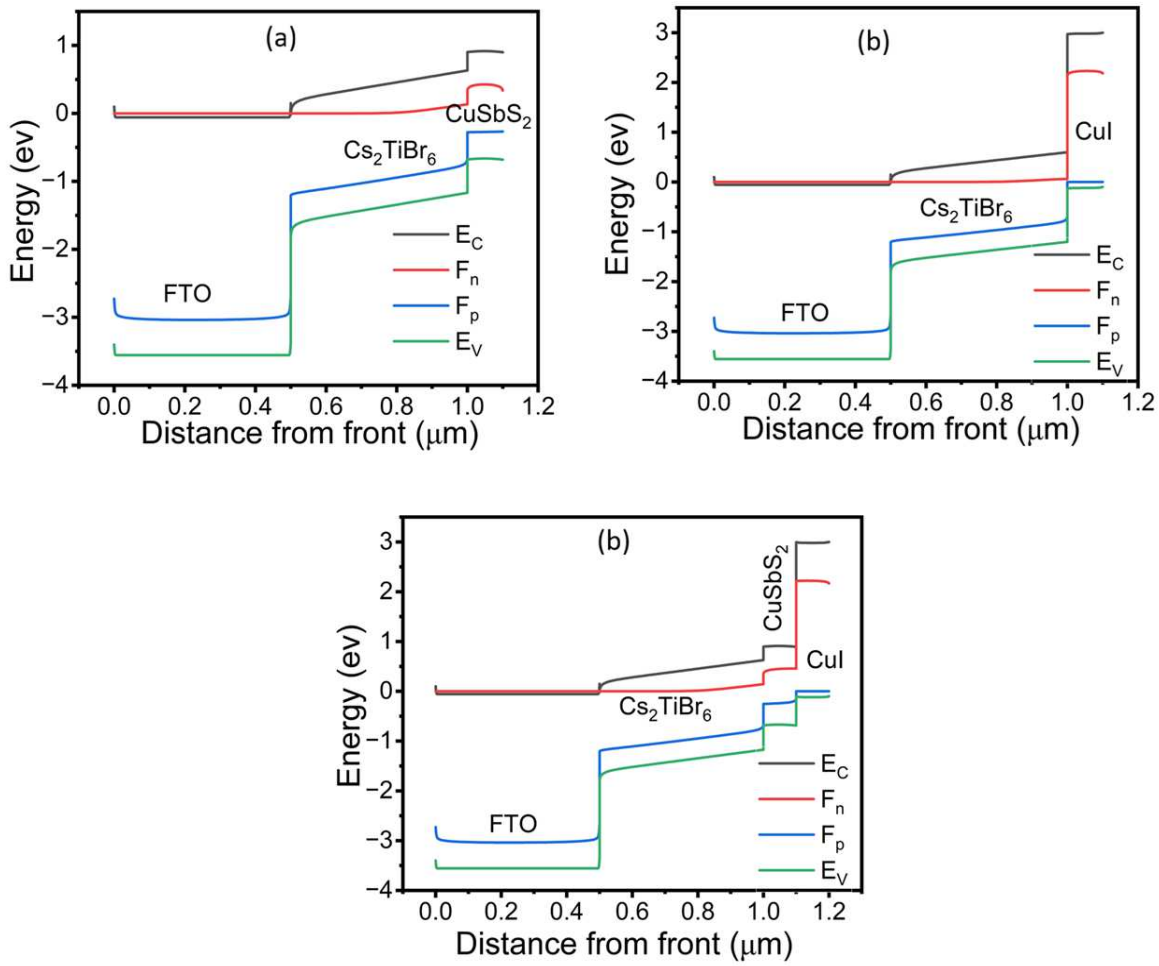


Figure 3. Graph of energy band for the PSC utilizing (a) $CuSbS_2$ HTL, (b) CuI HTL, (c) $CuSbS_2$ /CuI double HTL.

3.2 Influence of thickness of the absorber layer

The thickness of the Cs_2TiBr_6 absorber strongly has strong influence on the optical absorption, carrier transport, and recombination processes in the ETL-free PSC. As presented in Figs. 4 & 5, increasing the absorber thickness from 0.60 to 1.40 µm caused the V_{OC} to remain nearly constant at 0.80 V, while the J_{SC} increased slightly from 19.38 to 20.21 mA/cm^2. Conversely, the FF decreased continuously from 76.06 to 64.92%, leading to a gradual reduction in PCE from 11.81 to 10.49%. These results demonstrate that the device performance was controlled by the

competition between improved photon harvesting and increased electrical losses as the absorber thickness increased.

The slight improvement in J_{SC} originated from enhanced optical absorption in the thicker Cs_2TiBr_6 absorber layer. According to the Beer-Lambert law, increasing the absorber thickness increased the optical path length, thereby enabling greater absorption of incident photons, particularly those with energies close to the absorber bandgap. This behaviour is confirmed by the QE spectra (Fig. 4b). As the absorber thickness increases, the QE became progressively higher in the long-wavelength region between approximately 600 and 700 nm, indicating improved generation of carriers by photons with larger penetration depths. In contrast, the QE below approximately 550 nm remains almost identical for all thicknesses because high-energy photons were already absorbed efficiently within the front region of the absorber.

Unlike J_{SC}, the V_{OC} remained essentially unchanged (Fig. 5) throughout the investigated thickness range. Since the absorber doping concentration, defect density, and energy-band alignment remained constant, the built-in potential and dark saturation current (Eq. 8) [38] experienced negligible variation with thickness. As a result, the quasi-Fermi level splitting under illumination remained nearly constant, producing an invariant V_{OC} of ~0.80 V.

$$V_{OC} = \frac{nkT}{q} \ln\left(\frac{J_{ph}}{J_0} + 1\right), \qquad 8$$

where J_{ph} is the photogenerated current, J_0 the dark saturation current, n the ideality factor, q is electron charge, k is Boltzmann constant, and T is temperature.

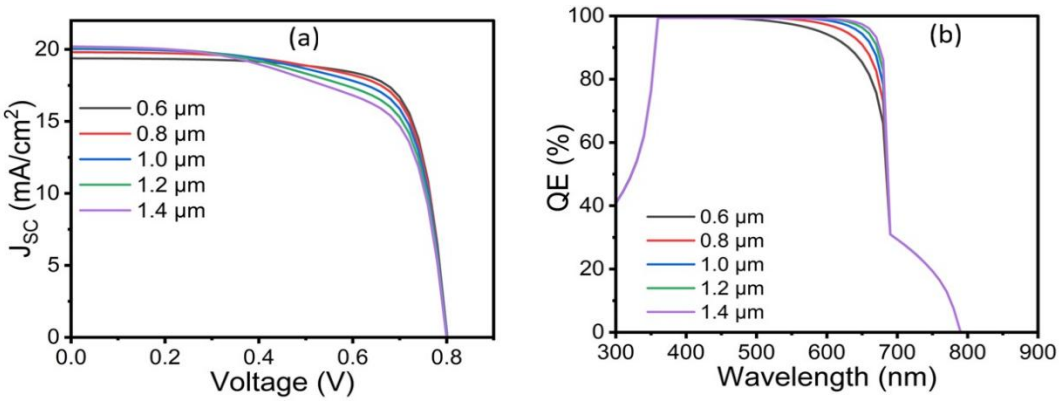


Figure 4. (a) J-V characteristic with varying absorber layer thickness, (b) QE plots.

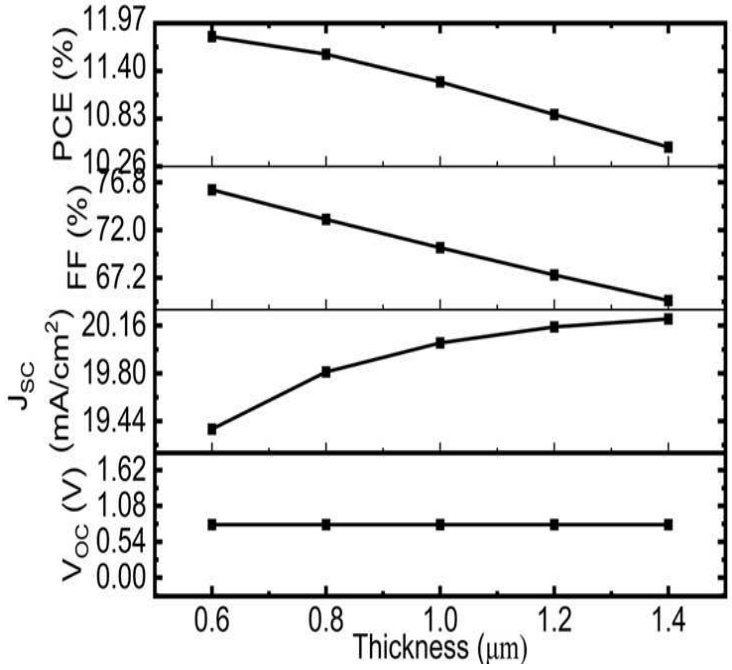


Figure 5. Dependence of V_{OC}, J_{SC}, FF and PCE on absorber layer thickness.

The progressive reduction in FF with increasing thickness indicated that electrical transport rather than optical absorption became the principal limitation to device performance. As the Cs_2TiBr_6 layer increased in thickness, photogenerated electrons and holes would travel longer distances before reaching their respective contacts. Because Cs_2TiBr_6 exhibits limited charge-carrier mobilities and limited carrier lifetimes, the longer transport distance increased the probability of Shockley-Read-Hall recombination within the absorber before charge extraction.

The extended carrier transfer distance also increased the internal resistive loss and impeded electric-field-assisted carrier collection, causing increased carrier accumulation inside the absorber layer. These effects were reflected in the J-V characteristics (Fig. 4a), where the thicker absorbers exhibited progressively greater curvature near the maximum-power-point region, characteristic of increased recombination and reduced charge collection efficiency. The degradation of the diode characteristics therefore manifested as a continuous decrease in FF from 76.06 to 64.92%. These results indicate that an absorber thickness of approximately 0.60 μm provides the optimal balance between efficient light absorption, short carrier transport distance, reduced recombination losses, and efficient charge collection for the proposed ETL-free Cs_2TiBr_6 PSC.

3.3 Impact of thickness of the $CuSbS_2$ HTL layer

The thickness of the $CuSbS_2$ HTL play an important role in controlling rear-contact selectivity, interfacial recombination, hole extraction, and carrier collection in the ETL-free FTO/Cs_2TiBr_6/$CuSbS_2$/CuI/Au device. As the $CuSbS_2$ thickness increased from 0.20 to 1.20 μm, the V_{OC} improved from 0.80 to 0.83 V, while the J_{SC} increased from 20.75 to 23.17 mA/cm^2 (Figs. 6 & 7). The FF first increased sharply from 67.40 at 0.20 μm to above 73% at 0.40 μm, after which it remained nearly stable. Therefore, the PCE increased continuously from 11.18 to 13.98%, indicating that thicker $CuSbS_2$ enhanced the electrical quality of the rear interface without introducing serious resistive losses within the investigated range. The continues increase in the JSC and PCE with $CuSbS_2$ thickness indicate its dual functions as HTL and a secondary/ supporting absorber layer.

The improvement in V_{OC} was mainly associated with reduced rear-interface recombination. $CuSbS_2$ formed a favorable hole-selective contact with Cs_2TiBr_6 because its valence-band position supported hole extraction, while its conduction-band offset acted as an electron-blocking barrier. At very low thickness, the $CuSbS_2$ layer may not provide complete coverage or sufficient band bending at the absorber/HTL interface, allowing electron leakage toward the rear contact and increasing Shockley-Read-Hall recombination. As the $CuSbS_2$ layer became thicker, it provided a more continuous and effective hole-selective contact, strengthened the back-surface-field effect, and suppressed minority-carrier recombination. This lowered the recombination current and increased the quasi-Fermi-level splitting, which explain the increase in V_{OC} from 0.80 to 0.83 V.

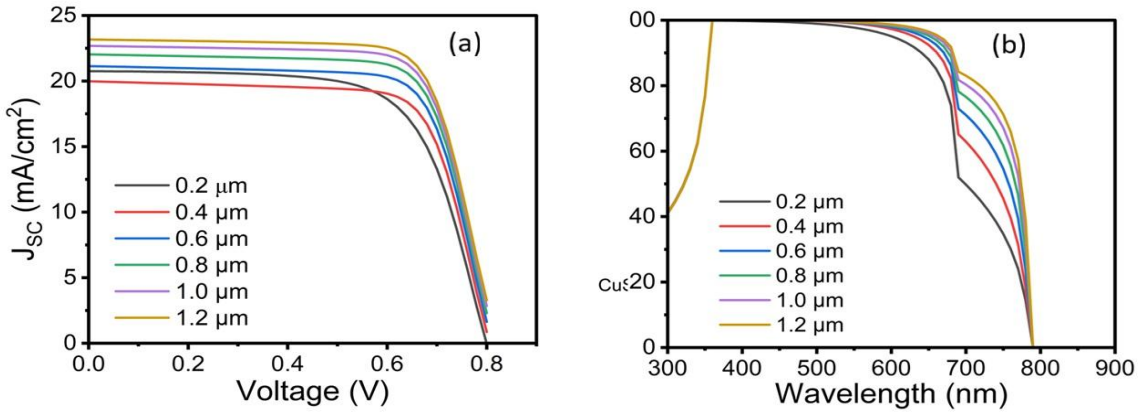


Figure 6. (a) J-V curves with varying $CuSbS_2$ HTL thickness, (b) QE plots.

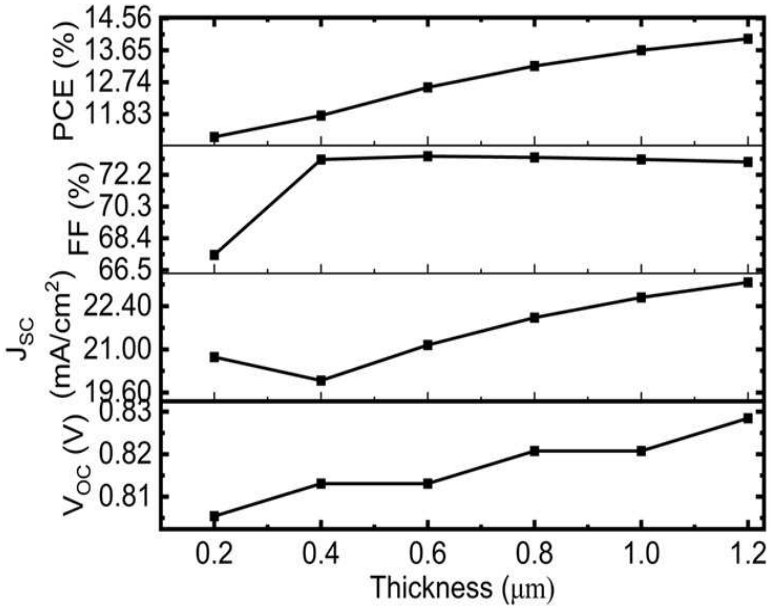


Figure 7. Dependence of V_{OC}, J_{SC}, FF and PCE on $CuSbS_2$ HTL thickness.

The rise in J_{SC} is strongly supported by the QE spectra (Fig. 6b). As the $CuSbS_2$ thickness increased, the QE response improved markedly in the long-wavelength region close to the absorption edge. This indicated that thicker $CuSbS_2$ enhanced the collection of carriers generated deeper in the Cs_2TiBr_6 absorber, particularly near the rear side of the device where long-wavelength photons were absorbed. The improved QE between approximately 650 and 780 nm suggested that a thicker $CuSbS_2$ layer strengthened rear-side carrier selectivity and reduced

recombination losses for carriers generated near the absorber/HTL interface. Thus, the observed increase in J_{SC} is not mainly due to $CuSbS_2$ absorbing more useful photons, but rather due to improved carrier collection and reduced rear-interface recombination.

The J-V curves in (Fig. 6a) further confirm this interpretation. The J_{SC} increased systematically with $CuSbS_2$ thickness, while the voltage at which the curves bend toward open circuit also shifted slightly upward. This reflected improved diode quality and reduced recombination losses. The very low FF at 0.20 µm suggested that the $CuSbS_2$ layer was too thin to form an efficient rear selective contact, leading to incomplete hole extraction, enhanced interfacial recombination, and possible leakage pathways. When the thickness increased to 0.40 µm, FF rose sharply to 73.11%, indicating the formation of a more effective and continuous HTL. Beyond this thickness, FF remained nearly constant, showing that additional $CuSbS_2$ does not introduce significant series resistance because the layer remained sufficiently conductive for hole transport. Therefore, the optimum $CuSbS_2$ thickness is 1.20 µm, where the device achieved the highest V_{OC}, J_{SC}, FF, and PCE of 0.83 V, 23.17 mA/cm^2, and 13.98% without significant FF deterioration.

3.4 Impact of thickness of the CuI HTL layer

The effect of CuI thickness on the photovoltaic response of the ETL-free FTO/Cs_2TiBr_6/$CuSbS_2$/CuI/Au device is almost negligible within the investigated range of 0.02–0.10 µm (Figs. 8 & 9). The V_{OC} remained fixed at 0.80 V, J_{SC} remained constant at 19.03 mA/cm^2, and the FF varied only slightly from 77.71 to 77.67%. As a result, the PCE remained practically unchanged at 11.84–11.86%. This indicated that once a thin and continuous CuI layer was formed, further increase in its thickness did not significantly modify the optical or electrical behaviour of the device.

The unchanged V_{OC} indicated that the recombination dynamics and quasi-Fermi level splitting were not controlled by the bulk thickness of CuI in this range. CuI mainly acted as a rear hole-selective and electron-blocking layer. Its large conduction-band offset with Cs_2TiBr_6 suppressed electron leakage toward the back contact, while its valence-band alignment supported hole transport through the rear side of the device. Once the CuI layer was sufficiently continuous, the interfacial recombination rate was determined primarily by the quality of the Cs_2TiBr_6/$CuSbS_2$

and $CuSbS_2$/CuI interfaces, rather than by the physical thickness of CuI. This explained why varying CuI thickness did not appreciably change V_{OC}.

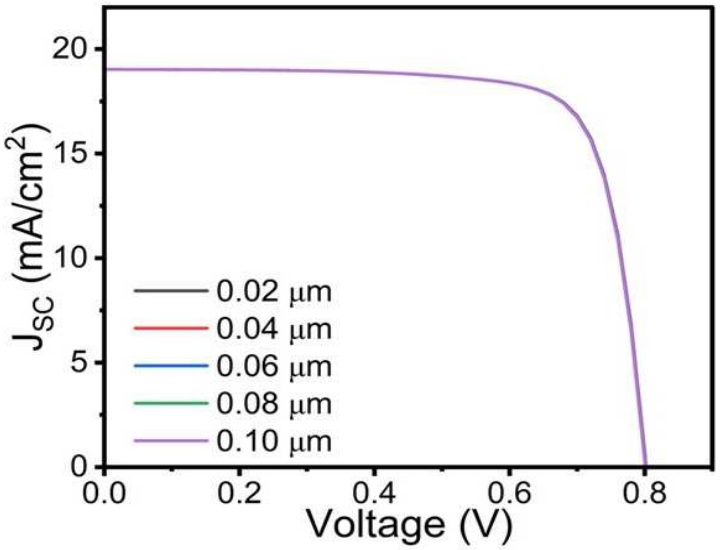


Figure 8. J-V characteristics with varying CuI HTL layer thickness.

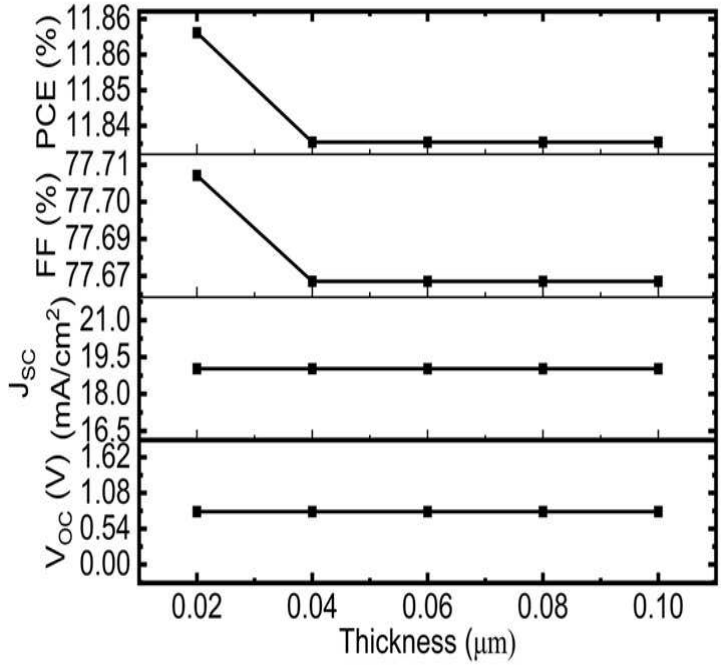


Figure 9. Dependence of V_{OC}, J_{SC}, FF and PCE on CuI HTL layer thickness.

The curves for all CuI thicknesses (Fig. 8) were superimposed, indicating identical diode behaviour, similar light absorption and carrier extraction efficiency, and negligible change in resistive losses. The very small reduction in FF from 77.71% at 0.02 μm to 77.67% at higher thicknesses is too small to indicate any meaningful degradation. It suggested that CuI remained sufficiently conductive for hole transport over the entire thickness range and does not introduce significant series resistance. The results showed that the 0.02 μm-thick layer was sufficient to provide effective rear-contact selectivity, while thicker CuI layers offered no additional performance advantage. Therefore, the thinnest CuI layer is preferable from a practical fabrication viewpoint because it reduces material usage, processing time, and possible resistive losses while maintaining essentially the same photovoltaic performance**.**

3.5 Impact of carrier concentration of $CuSbS_2$ layer

The acceptor carrier concentration of the $CuSbS_2$ hole transport layer strongly influenced the electrical behaviour of the ETL-free FTO/Cs_2TiBr_6/$CuSbS_2$/CuI/Au PSC by controlling the HTL conductivity, band bending, built-in electric field, hole extraction, and interfacial recombination. As shown in Table 4, increasing the $CuSbS_2$ acceptor carrier density from 10^{16} to 10^{19} cm^{-3} improved the PCE from 11.84 to 16.92%. This improvement was mainly driven by the strong enhancement in V_{OC} and FF, which increased to 1.09 V and 87.76%, respectively, at 10^{19} cm^{-3}. However, J_{SC} decreased from 19.03 to 17.74 mA/cm^2, indicating that the efficiency improvement was not due to enhanced photogeneration but rather to improved electrical selectivity and reduced recombination losses.

At the lowest acceptor concentration of 10^{16} cm^{-3}, $CuSbS_2$ had relatively low hole density and limited electrical conductivity. This increased resistive losses during hole transport and weakened band bending at the Cs_2TiBr_6/$CuSbS_2$ interface. Under this condition, the built-in electric field was insufficient to efficiently sweep holes toward the back contact, allowing carrier accumulation and recombination near the absorber/HTL interface. As a result, the device exhibited modest V_{OC} of 0.80 V, FF of 77.67%, and PCE of 11.84%.

Table 4. Influence of $CuSbS_2$ acceptor carrier concentration on photovoltaic performance

Acceptor carrier concentration of $CuSbS_2$ layer (cm^{-3})	Voc (V)	Jsc (mA/cm^2)	FF (%)	PCE (%)
10^{16}	0.80	19.03	77.67	11.84
10^{17}	-	17.16	-	12.53
10^{18}	-	17.54	-	15.22
10^{19}	1.09	17.74	87.76	16.92

When the $CuSbS_2$ acceptor density was increased, the hole concentration in the HTL increased, which improved its conductivity and reduced series resistance. More importantly, higher p-type doping strengthened the built-in electric field at the $Cs_2TiBr_6/CuSbS_2$ heterojunction and narrowed the depletion region inside the $CuSbS_2$ layer. This improved hole selectivity and facilitated faster hole extraction from the absorber. The enhanced band bending also suppressed electron back-transfer toward the rear contact, thereby reducing interfacial Shockley-Read-Hall recombination. These effects explain the strong rise in V_{OC} and FF at high doping concentration.

The reduction in J_{SC} from 19.03 to 17.74 mA/cm^2 at higher acceptor concentration could arise from increased band bending, altered carrier distribution near the absorber/HTL interface, or enhanced free-carrier-related losses in the heavily doped $CuSbS_2$ layer. Nevertheless, this current loss was outweighed by the much larger gains in V_{OC} and FF. Therefore, the PCE improved substantially as the $CuSbS_2$ acceptor density increased. This confirmed that proper p-type doping of the $CuSbS_2$ HTL is essential for maximizing charge selectivity and reducing recombination losses in ETL-free Cs_2TiBr_6 PSC.

3.6 Impact of acceptor carrier concentration in CuI layer

The acceptor carrier concentration of the CuI hole transport layer showed a moderate but physically meaningful influence on the photovoltaic performance of the ETL-free $FTO/Cs_2TiBr_6/CuSbS_2/CuI/Au$ PSC. As the CuI acceptor concentration increased from 1×10^{17} to 9×10^{17} cm^{-3}, the V_{OC} increased from 0.80 to 0.83 V, while the FF improved from 77.67 to 78.54% (Fig. 10). Since J_{SC} remained essentially unchanged at 19.03 mA/cm^2, the PCE rose progressively from 11.84 to 12.37%. This suggested that CuI doping primarily enhanced the electrical quality of the rear contact rather than the photocarrier generation.

The increase in V_{OC} was caused by enhanced band bending and boosted built-in potential at the rear HTL/contact region. At low CuI acceptor concentration, the hole density in CuI was comparatively low, which could increase resistive losses and weaken the hole-selective field. As the acceptor concentration increased, the CuI layer exhibited more conductivity and its Fermi level shifted towards the valence-band edge. This facilitated hole transfer from $CuSbS_2$ into CuI and suppressed carrier accumulation at the $CuSbS_2$/CuI interface. The reduction in interfacial carrier accumulation lowered Shockley-Read-Hall recombination, enhanced quasi-Fermi level splitting, and therefore increased the V_{OC}.

The improvement in FF could also be linked to better hole transport. Higher CuI acceptor concentration reduced the resistivity of the HTL and improved contact selectivity with the Au electrode. This decreased the effective series resistance and improved the squareness of the J-V curve (Fig. 10a). The gradual rightward shift of the J-V curves with increased CuI doping confirmed improved diode quality and reduced recombination under forward bias. However, the FF improvement was modest because CuI already possessed high hole mobility and good conductivity at the lowest investigated doping concentration.

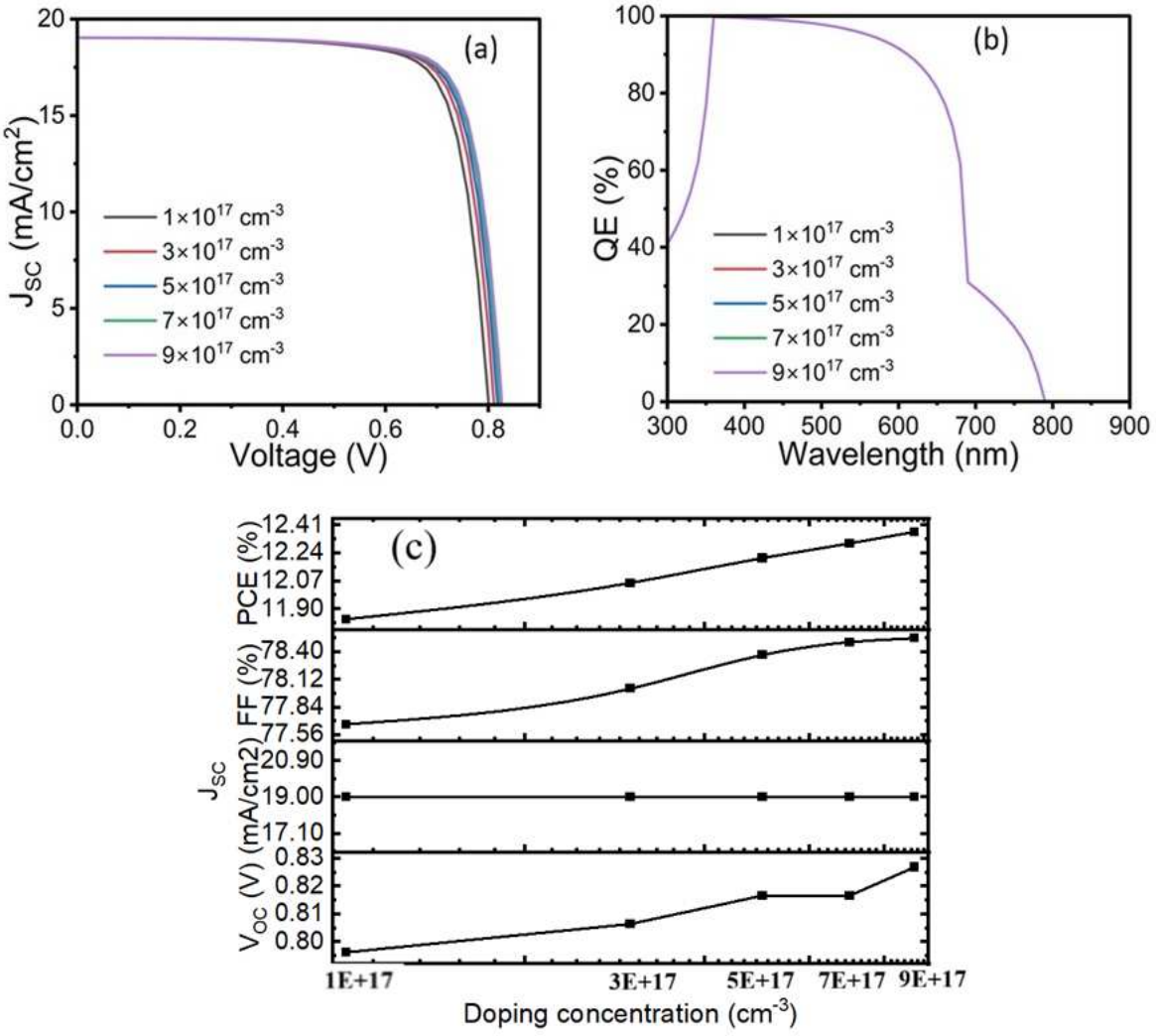


Figure 10. (a) J-V characteristic with varying acceptor carrier density of CuI HTL, (b) QE spectra, (c) Dependence of V_{OC}, J_{SC}, FF and PCE on acceptor carrier density of CuI HTL.

The constant J_{SC} is strongly supported by the QE spectra (Fig. 10b). The QE curves completely overlapped across the entire wavelength range, showing that CuI carrier concentration does not modify photon absorption or carrier generation in the Cs_2TiBr_6 absorber. This is expected because CuI is a wide-bandgap, transparent HTL and is positioned behind the absorber. Therefore, changing its acceptor density affected electrical transport and recombination, not the optical

absorption profile. This confirms that moderate p-type doping of CuI is beneficial for improving charge selectivity and rear-contact quality in ETL-free Cs_2TiBr_6 PSC.

3.7 Impact of defect density of absorber layer

The bulk defect density of the Cs_2TiBr_6 absorber showed a severe influence on the photovoltaic performance of the ETL-free FTO/Cs_2TiBr_6/$CuSbS_2$/CuI/Au PSC because defects introduced deep trap states that acted as non-radiative recombination centres. As the absorber defect density increased from 10^{14} to 10^{18} cm^{-3}, the PCE decreased sharply from 11.84 to 1.63% (Fig. 12). This degradation was mainly caused by the simultaneous reduction in J_{SC} and FF, while V_{OC} decreased more moderately from 0.80 to 0.74 V.

At a low defect density of 10^{14} cm^{-3}, the absorber maintained efficient carrier generation and extraction, giving J_{SC} (Fig. 11a), FF, and PCE of 19.03 mA/cm^2, 77.67%, and 11.84%. However, when the defect density increases to 10^{15} cm^{-3}, trap-assisted Shockley-Read-Hall recombination became stronger, reducing carrier lifetime (Eq. 9) [36] and lowering the FF to 59.41%. At 10^{16} cm^{-3} and 10^{17} cm^{-3} the recombination centres became sufficiently dense to strongly shorten the carrier diffusion length. As a result, many photogenerated carriers recombined before reaching the selective contacts, causing J_{SC} to fall from 17.74 to 10.23 mA/cm^2 (Fig. 1a) and PCE to collapse from 4.31 to 1.78%.

$$\tau_{SRH} = \frac{1}{\sigma v_{it} N_t}, \qquad 9$$

Where τ_{SRH} is carrier lifetime, σ is the capture cross-section, v_{it} is carrier thermal velocity, N_t is defect density. Carrier lifetime and diffusion length ($L=\sqrt{D\tau}$) decreased as defect density increases, resulting to enhanced non-radiative recombination losses.

The QE spectra (Fig. 11b) support this recombination-based interpretation. At lower defect densities, the device maintained high QE across the visible region, suggesting that most absorbed photons were successfully converted into extracted carriers. As the defect density increased, the QE decreased substantially, particularly in the long-wavelength region near the optical absorption edge. This occurred because long-wavelength photons penetrated deeper into the Cs_2TiBr_6 absorber layer and generated carriers farther from the collecting interface. At high trap density, these carriers travelled longer distances through a defect-rich absorber layer and were more likely to recombine before extraction. This reduction in QE directly explains the sharp loss in J_{SC}.

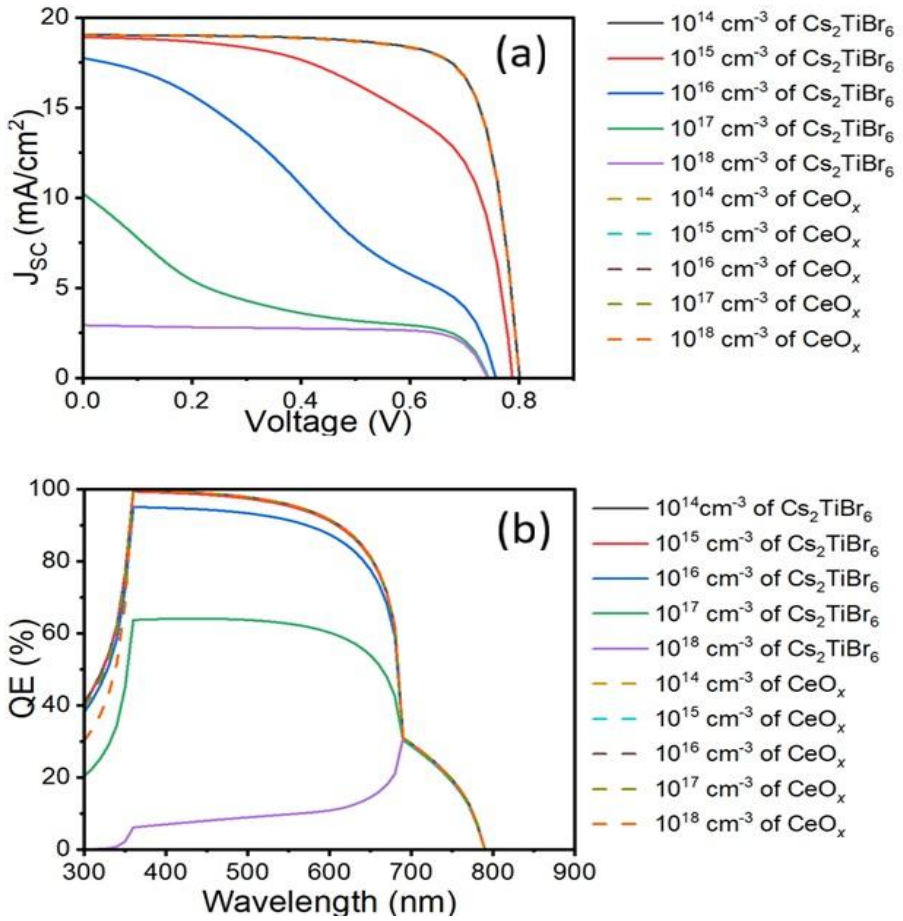


Figure 11. (a) J-V curves with varying defect density of absorber layer, (b) QE plots.

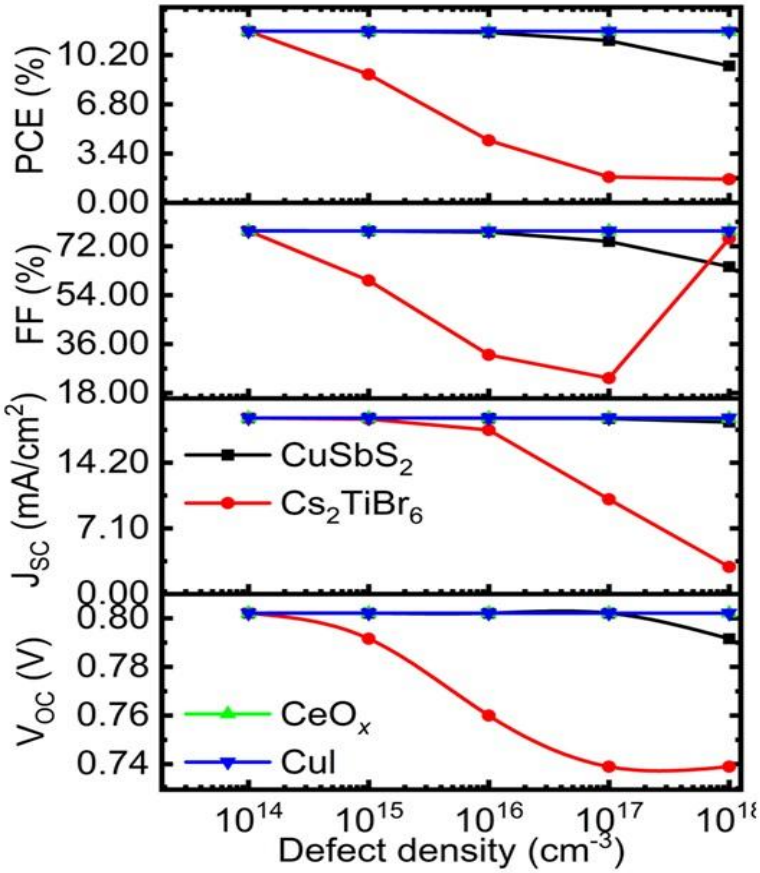


Figure 12. Dependence of V_{OC}, J_{SC}, FF and PCE on defect density of absorber layer.

.

The J-V characteristics (Fig. 11a) also demonstrated progressive degradation as the absorber defect density increased. Higher trap density boosted the dark recombination current, suppressed the diode quality, and produced severe curvature in the J-V response. This explained the strong decline in FF, particularly at 10^{15}–10^{17} cm^{-3}. The apparent recovery of FF at defect density of 10^{18} cm^{-3} should not be interpreted as enhanced device quality. At this high defect density, the photocurrent was already severely reduced (J_{SC} = 2.93 mA/cm^2), so the J-V curve became current-starved. The remarkable FF could be traced to a mathematical consequence of the distorted low-current curve rather than a real improvement in carrier transport. To sustain efficient operation, the absorber bulk defect density should be kept close to 10^{14} cm^{-3}, where recombination losses were minimized and carrier collection remained efficient.

3.8 Influence of defect density of $CuSbS_2$ layer

The defect density of the $CuSbS_2$ HTL demonstrated a relatively weak but physically meaningful effect on the PSC. As the $CuSbS_2$ defect density increases from 10^{14} to 10^{17} cm^{-3}, the V_{OC} remained constant at 0.80 V (Fig. 12), while J_{SC} decreases only slightly from 19.03 to 18.98 mA/cm^2 (Fig. 13a). However, the FF decreases from 77.71 to 73.78%, causing the PCE to decline from 11.84 to 11.19% (Fig. 12). This indicated that defects in $CuSbS_2$ mainly affected charge transport and diode quality rather than optical absorption or the maximum photovoltage.

The unchanged V_{OC} showed that the dominant recombination losses were not controlled by the bulk $CuSbS_2$ layer. Since $CuSbS_2$ is located behind the Cs_2TiBr_6 absorber and functions mainly as a hole-selective contact, its bulk defects have limited influence on the quasi-Fermi level splitting inside the absorber. The constant V_{OC} therefore suggested that recombination in the absorber and at the absorber/HTL interface remained the primary factor determining the open-circuit voltage.

The slight decrease in J_{SC} (Fig. 13a) is consistent with the QE spectra in Fig. 13(b). The QE spectra for all $CuSbS_2$ defect densities overlapped across the visible wavelength range, showing that increasing $CuSbS_2$ defects did not significantly affect photon absorption or photogeneration in Cs_2TiBr_6. This is expected because $CuSbS_2$ is positioned at the rear side of the device and does not act as the main absorber. The very small reduction in J_{SC} at higher defect density was not optical in origin, but resulted from slightly poorer carrier collection near the rear interface, where defects could promote trap-assisted recombination of holes transported through the HTL.

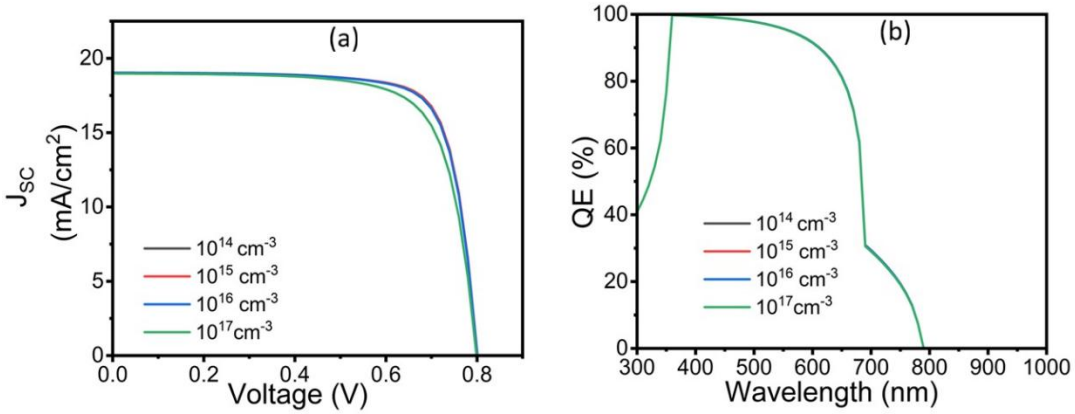


Figure 13. (a) J-V curves with varying defect density of $CuSbS_2$ layer**,** (b) QE spectra for $CuSbS_2$ layer.

The most noticeable effect appeared in the FF, which decreased as $CuSbS_2$ defect density increased. Defect states in $CuSbS_2$ can act as trap-assisted recombination centres and also reduce the effective hole mobility through trap-limited transport. Under forward bias, these traps increase recombination current, enhance carrier accumulation, and increase the effective series resistance of the rear contact. This caused the J-V curve in Fig. 13a to become less square at higher defect density, thereby reducing the FF. The fall in FF from 77.71 to 73.78% was a signature of degraded transport quality and enhanced recombination losses in the $CuSbS_2$ HTL.

3.9 Influence of bulk defect density of CuI layer

The bulk defect density of the CuI HTL exhibited a negligible impact on the photovoltaic performance of the PSC within the varied range of 10^{14}–10^{18} cm^{-3}. As shown in Figs. 11 & 12, the V_{OC}, J_{SC}, FF, and PCE remained completely unchanged at 0.80 V, 19.03 mA/cm^2, 77.67%, and 11.84%, respectively (Fig. 12). This indicated that bulk defects in CuI did not act as dominant recombination or transport-limiting centres in the device.

This weak sensitivity could be explained by the role and position of CuI in the cell. CuI is located behind the absorber and $CuSbS_2$ layer, where it functions mainly as a rear hole-selective contact rather than as a photon-absorbing or carrier-generation layer. Because Cs_2TiBr_6 is the main absorber, changes in CuI defect density did not alter the photogeneration rate. In addition, CuI has

a wide bandgap of about 3.1 eV, which makes it highly transparent in the visible region and prevented parasitic absorption. Therefore, J_{SC} (Fig. 11a) remained unchanged even when the CuI defect density was increased. Since CuI is separated from the absorber by $CuSbS_2$ in the bilayer architecture, defects inside CuI had limited direct interaction with photogenerated minority carriers. Moreover, the large conduction-band offset of CuI provided a strong barrier against electron leakage into the rear contact. Because very few electrons reached the CuI layer, trap-assisted Shockley-Read-Hall recombination inside CuI remained minimal, even at high defect density.

The unchanged FF further showed that CuI maintained sufficient hole-transport capability throughout the investigated defect range (Fig. 12). Although defects can, in principle, introduce trap-assisted hopping, reduce mobility, and increase series resistance, the simulated CuI layer was thin and had adequate hole conductivity. As a result, increasing its defect density did not produce measurable resistive losses or distortion in the J-V characteristics. Therefore, while good CuI film quality remains desirable for practical device stability, the simulation indicated that the device can tolerate CuI defect densities as high as 10^{18} cm^{-3} without performance degradation.

3.10 Impact of defect density of $Cs_2TiBr_6/CuSbS_2$ interface

The interface defect density at the $Cs_2TiBr_6/CuSbS_2$ interface has a significant influence on the photovoltaic performance of the ETL-free PSC because this interface control hole extraction, electron blocking, and interfacial recombination. As the interface defect density rose from 10^{10} to 10^{15} cm^{-2}, the V_{OC} declined from 0.82 to 0.73 V, while the FF fell significantly from 78.57 to 62.85% (Fig. 14). As a result, the PCE declined from 12.29 to 8.73%. In contrast, J_{SC} remained almost unchanged, decreasing marginally from 19.03 to 18.98 mA/cm^2, suggesting that the degradation was primarily electrical rather than optical.

At low interface defect densities of 10^{10} to 10^{12} cm^{-2}, the device maintained an identical V_{OC} values of ≈ 0.82 V, J_{SC} of 19.03 mA/cm^2, FF ≈ 78.58%, and PCE of 12.23–12.29%. This indicated that the $Cs_2TiBr_6/CuSbS_2$ interface was sufficiently passivated, allowing efficient hole extraction from the absorber into $CuSbS_2$. In this regime, the conduction-band offset at the interface blocked electron leakage toward the rear contact, while the valence-band alignment

supported hole transport. As a result, interfacial Shockley-Read-Hall recombination remained weak, and the quasi-Fermi level splitting was preserved.

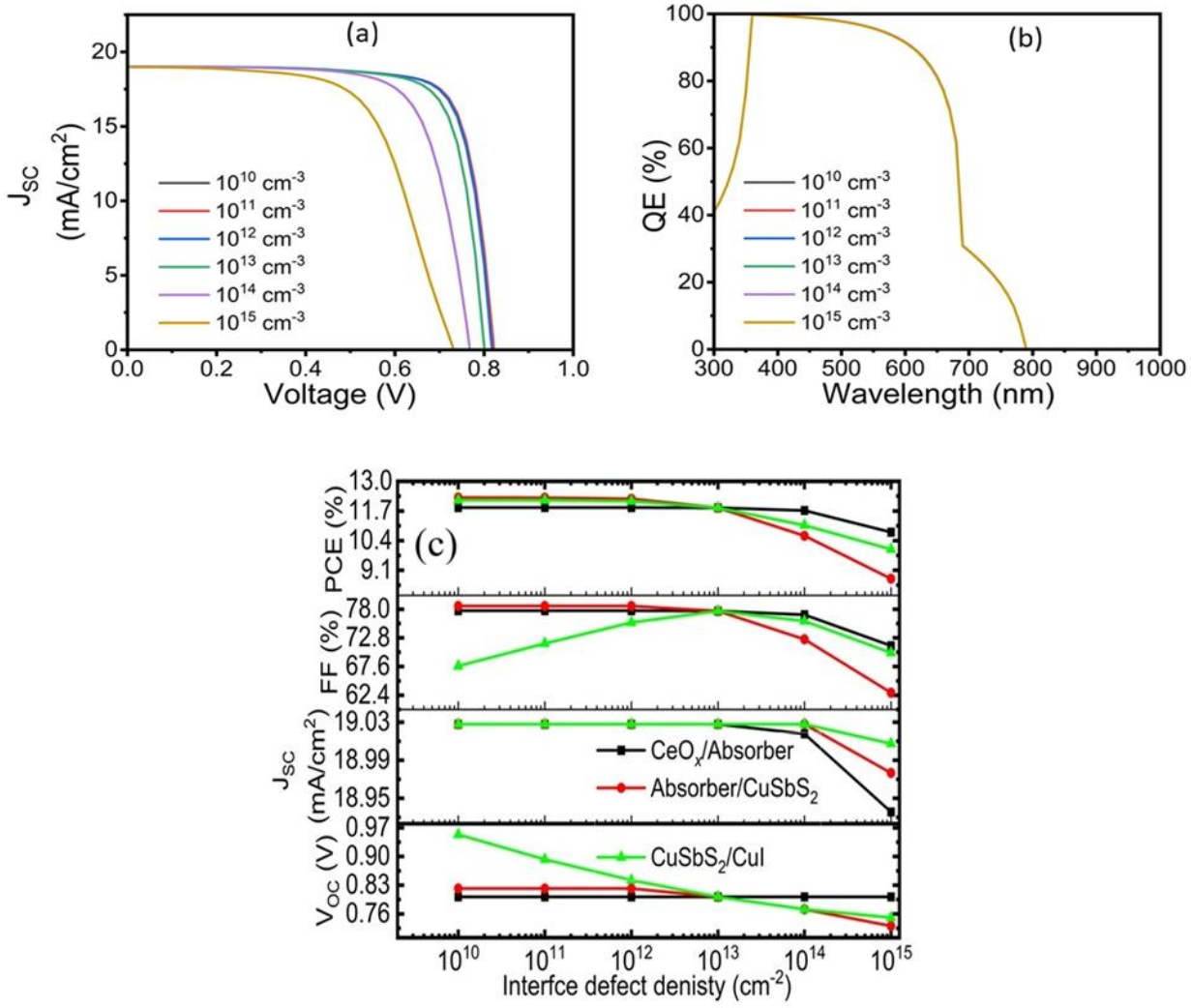


Figure 14. (a) J-V characteristics with varying interface defect density at absorber/$SuSbS_2$, (b) QE spectra, (c) Dependence of V_{OC}, J_{SC}, FF and PCE on interface defect density at absorber/$CuSbS_2$ and $CuSbS_2$/CuI.

An increase in interface defect density to 10^{13} cm^2 resulted in performance degradation, with V_{OC} decreased to 0.80 V and FF to 77.67%. The performance deterioration became more severe at higher densities of 10^{14} and 10^{15} cm^2. These defect states served as recombination-active

traps at the Cs_2TiBr_6/$CuSbS_2$ interface, capturing electrons and holes before they could be selectively collected. This improved the interfacial recombination velocity, boosted the dark saturation current, and reduced the quasi-Fermi level splitting under illumination. The direct consequence was the reduction in V_{OC}. At the same time, enhanced recombination under forward bias distorted the J-V curve near the maximum-power point, causing a substantial decline in FF.

The nearly constant J_{SC} showed that increasing the interface defect density did not significantly alter photon absorption inside Cs_2TiBr_6. This interpretation is supported by the QE spectra (Fig. 14b), where the curves overlapped over the visible wavelength range. Since the optical generation profile was unchanged, the photocurrent remained almost constant. The slight decrease in J_{SC} at the highest defect density was likely caused by increased recombination of carriers generated near the rear Cs_2TiBr_6/$CuSbS_2$interface, particularly those generated by longer-wavelength photons that penetrated deeper into the absorber. Therefore, effective interface passivation and careful control of the Cs_2TiBr_6/$CuSbS_2$ junction are essential for maintaining high diode quality and efficient operation in ETL-free Cs_2TiBr_6 PSC.

3.11 Effect of defect density at $CuSbS_2$/CuI interface

The defect density at the $CuSbS_2$/CuI interface has a distinctive influence on the photovoltaic behaviour of the ETL-free FTO/Cs_2TiBr_6/$CuSbS_2$/CuI/Au device because this interface lies within the bilayer hole-transport region and controls hole transfer from $CuSbS_2$ into CuI. Unlike absorber-related defects, which mainly suppress photocurrent, defects at the $CuSbS_2$/CuI interface primarily alter the balance between interfacial recombination, contact resistance, quasi-Fermi level splitting, and fill factor.

As the $CuSbS_2$/CuI interface defect density increases from 10^{10} to 10^{15} cm^{-2}, the VOC decreases continuously from 0.95 to 0.75 V, indicating increasing non-radiative recombination at the HTL/HTL junction. Interface traps capture holes transported from $CuSbS_2$ and electrons that leak toward the rear side, thereby increasing Shockley–Read–Hall recombination. This raises the dark saturation current and reduces quasi-Fermi level splitting, causing the observed voltage loss.

Interestingly, the FF initially increases from 67.69% at 10^{10} cm^{-2} to 77.67% at 10^{13} cm^{-2}, before decreasing again to 70.09% at 10^{15} cm^{-2}. This non-monotonic behaviour indicates a competition between contact transport and recombination. At extremely low interface defect density, the

$CuSbS_2$/CuI interface might behave as a poorly conducting or partially blocking heterointerface because hole transfer occurred across a sharp energetic discontinuity with limited interfacial tunnelling pathways. This produced substantial contact resistance and a lower FF. A moderate density of interfacial states could improve charge transfer by assisting hole transfer across the $CuSbS_2$/CuI interface and reducing the interfacial transport barrier, thereby improving the squareness of the J-V curve. Nevertheless, when the defect density became too high, these same states became dominant recombination centres, boosting recombination current and lowering both V_{OC} and FF.

The nearly constant J_{SC} from 19.03 to 19.01 mA/cm^2 showed that the $CuSbS_2$/CuI interface defect density did not significantly influence optical absorption or photogeneration. This interpretation is supported by the QE spectra (Fig. 15b), where the curves are completely overlapped across the visible spectrum. Since $CuSbS_2$/CuI is a buried HTL/HTL interface located behind the Cs_2TiBr_6 absorber layer. Therefore, changing its defect density did not alter the number of photons absorbed in the perovskite absorber. The negligible change in QE confirmed that the photocurrent was controlled by Cs_2TiBr_6 absorption and front-side carrier collection rather than by optical or generation changes at the HTL interface.

The J-V curves (Fig. 15a) confirmed that the major effect of increasing $CuSbS_2$/CuI interface defect density was electrical. The progressive leftward shift of the V_{OC} with increasing defect density reflects increasing recombination at the interface and reduced quasi-Fermi level splitting. At moderate defect densities, improved FF compensates for the decreasing V_{OC}, keeping the PCE nearly unchanged at about 12.1% for 10^{10}–10^{12} cm^{-2}. However, beyond 10^{13} cm^{-2}, recombination became dominant, and both V_{OC} and FF declined, reducing the PCE from 11.84 to 10.02%. These results demonstrate that careful engineering of the $CuSbS_2$/CuI interface is essential for optimizing the bilayer HTL in ETL-free Cs_2TiBr_6 PSCs.

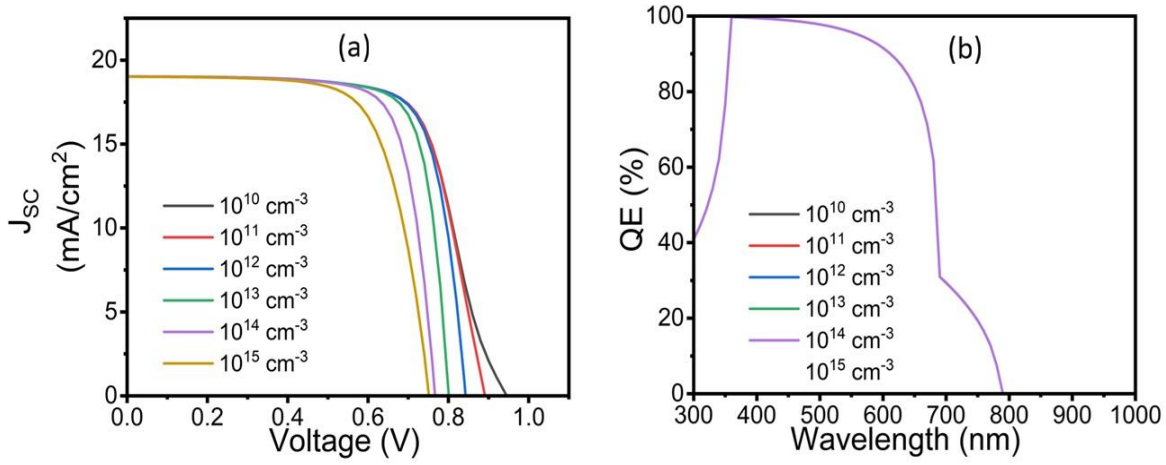


Figure 15. (a) J-V curves with varying defect density at $SuSbS_2$/CuI interface, (b) QE plots

3.12 Capture Cross-section of electron in the absorber layer

The electron capture cross-section of defects in the Cs_2TiBr_6 absorber is a crucial recombination parameter because it determines the probability that free electrons are captured by defect states and subsequently undergo Shockley-Read-Hall recombination [27, 39] A larger capture cross-section corresponds to a higher capture probability, shorter carrier lifetime, and larger non-radiative recombination. On the other hand, a smaller capture cross-section suppresses trap-assisted recombination and prolongs carrier lifetime [40, 41]. As shown in Fig. 15, reducing the electron capture cross-section from 1×10^{-15} to 1×10^{-19} cm^2 slightly improved the device performance. While V_{OC} remained constant at 0.80 V and J_{SC} increased only marginally from 19.03 to 19.04 mA/cm^2, the FF increased from 77.67 to 80.67%, leading to an increase in PCE from 11.84 to 12.33%.

The negligible variation in V_{OC} indicated that reducing the electron capture cross-section produced only a modest decrease in the recombination current. Since the absorber defect density, interface properties, and built-in potential remained unchanged. The quasi-Fermi level splitting was only weakly affected, resulting in an almost constant V_{OC}. The negligible increase in J_{SC} is consistent with the QE spectra (Fig. 15b). The QE curves completely overlapped throughout the visible wavelength range, indicating that changing the electron capture cross-section did not alter the optical absorption characteristics of the Cs_2TiBr_6 absorber.

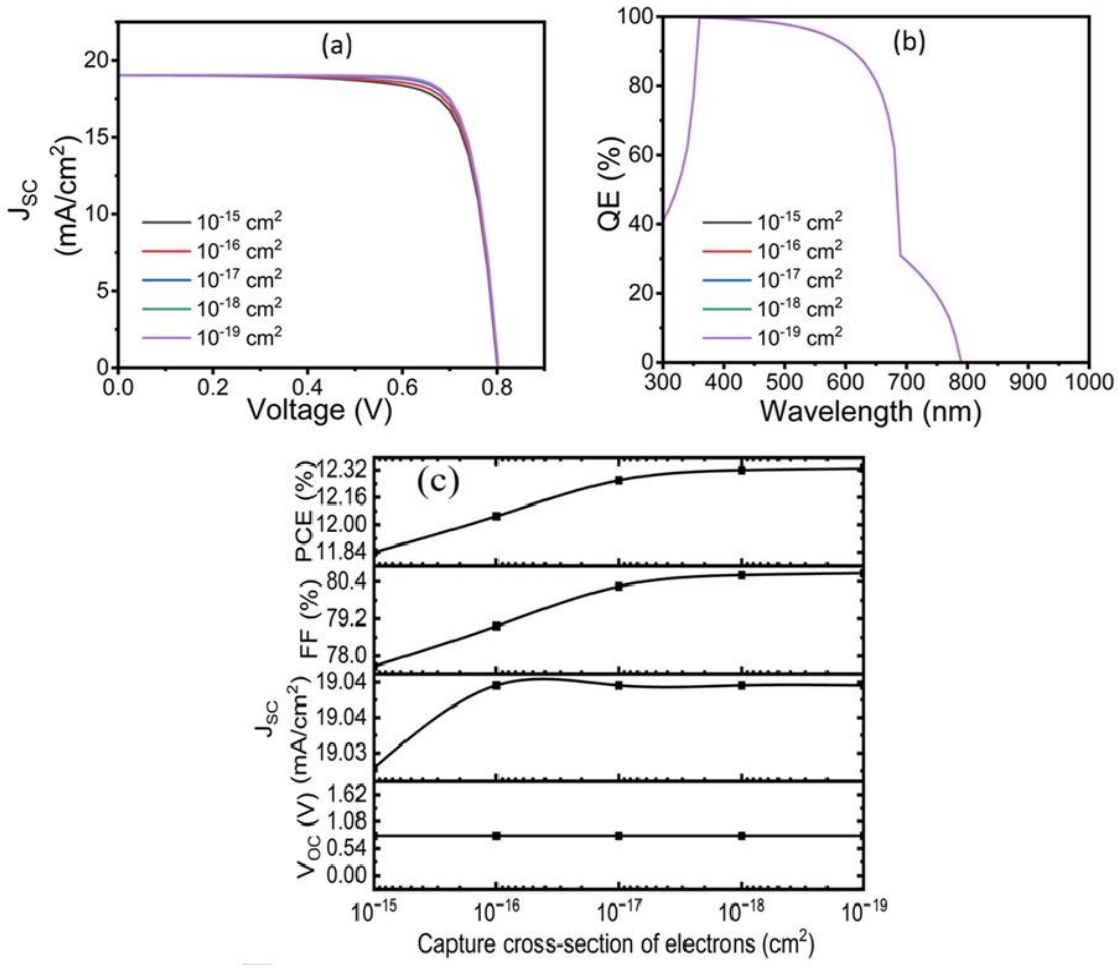


Figure 16. (a) J-V curves with varying capture cross section in the absorber layer, (b) QE spectra.

The most significant improvement occurred in the FF, which increased steadily as the capture cross-section decreased. A smaller electron capture cross-section lowered the probability of electron trapping at defect centres, thereby reducing Shockley-Read-Hall recombination within the absorber. The longer carrier lifetime enabled more efficient charge extraction and reduced carrier accumulation under forward bias. As a result, the recombination current decreased, the diode ideality improved, and the J-V characteristics became more rectangular (Fig. 16a). This improvement in diode quality is reflected by the progressive increase in FF from 77.67 to 80.67%.

According to the Shockley-Read-Hall recombination theory (Eq. 6), the carrier capture rate is directly proportional to the capture cross-section. Therefore, decreasing the electron capture cross-section effectively suppressed the recombination velocity of defect states, facilitated the minority-carrier lifetime, and boosted charge collection efficiency without altering the carrier generation profile. SInce recombination losses were mitigated while photon absorption remained constant, the improvement in device performance was primarily electrical rather than optical. These findings indicate that minimizing the electron capture probability of bulk defects is an effective strategy for improving the performance of ETL-free Cs_2TiBr_6 perovskite solar cells.

3.13 Influence of series resistance

Series resistance is a critical parasitic parameter in solar cells because it represents the combined ohmic resistance arising from the semiconductor layers, interfaces, transparent conducting electrode, metallic contacts, and carrier-transport pathways [42]. An increase in series resistance produces an additional voltage drop as photogenerated carriers flow through the device, thereby reducing the electrical power delivered to the external load [42, 43]. Figs. 17 & 18a showed that increasing series resistance from 0 to 4 $\Omega.cm^2$ had no observable influence on V_{OC} and J_{SC}, which remain constant at 0.80 V and 19.03 mA/cm^2, respectively. In contrast, the FF decreased continuously from 77.67% at 0 $\Omega.cm^2$ to 70.19% at 4 $\Omega.cm^2$, while the corresponding PCE decreased from 11.84 to 10.70%. Thus, the increase in series resistance caused an absolute FF loss of 7.48 percentage points and a PCE reduction of 1.14 percentage points, corresponding to approximately 9.6% of the initial PCE.

At short circuit (V= 0 V), the ($J.R_s$, where R_s is series resistance) voltage drop is small, so J_{SC} is essentially unaffected by series resistance (Eq. 10) [33, 36, 44]. At open circuit, the current is zero, eliminating the voltage drop across (R_s); therefore, V_{OC} is controlled mainly by carrier generation and recombination. Therefore, both J_{SC} and V_{OC} remained nearly constant over the investigated series resistance range.

$$J = J_{ph} - J_0\left[exp\left(\frac{q(V+JR_s)}{nkT}\right) - 1\right] - \frac{V+JR_s}{R_{sh}}, \qquad 10$$

where J_0 is reverse current, J represent output current, J_{ph} is photocurrent density, R_s denote series resistance, R_{sh} represent shunt resistance, T designate temperature, V is applied voltage, k is Boltzman constant, q is charge, , and n is ideality factor.

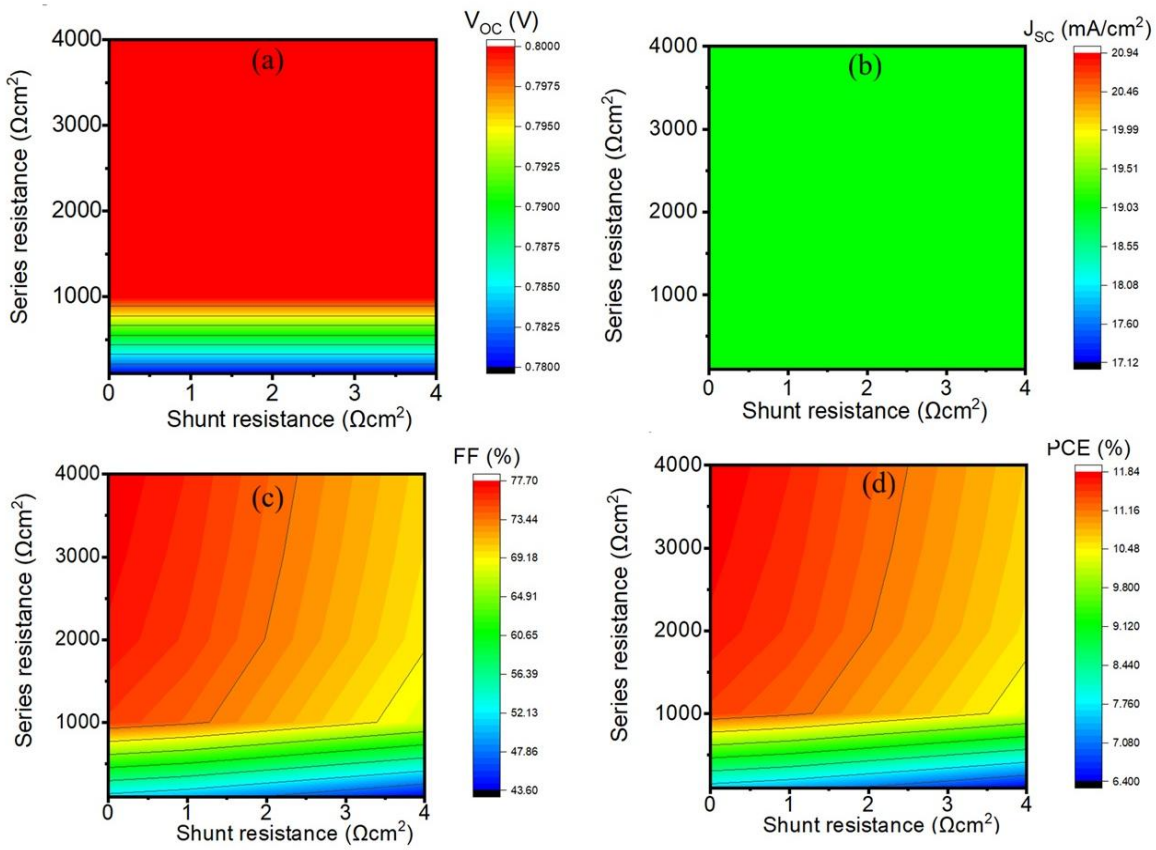


Figure 17. (a) Contour plots for (a) V_{OC}, (b) J_{SC}, (c) FF, (d) PCE for series and shunt resistance

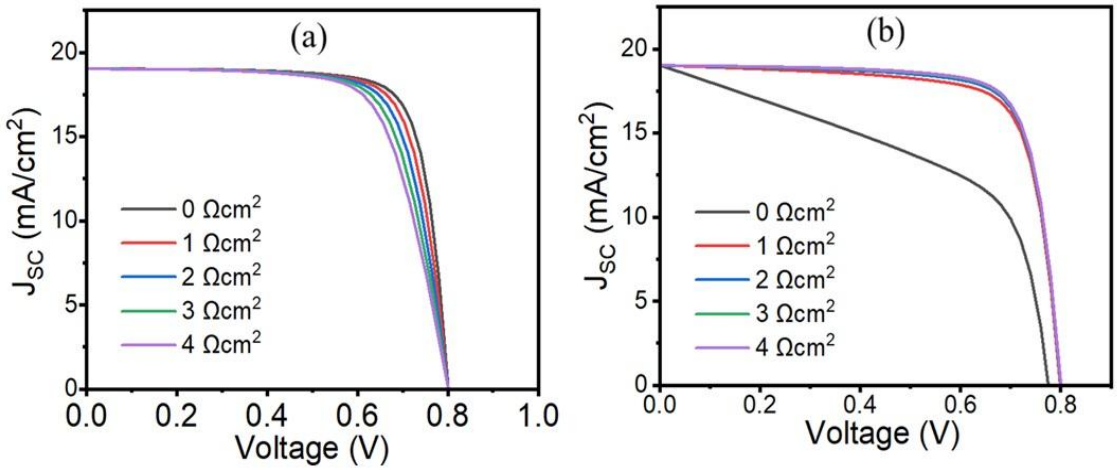


Figure 18. J-V characteristics for the varied (a) Series resistance, (b) Shunt resistance.

The major influence of series resistance was observed around the maximum-power region of the J-V characteristic, where a substantial current flowed through the device. As series resistance increased, the associated ohmic voltage loss, ($J.R_s$), became progressively larger, reducing the voltage available at the external terminals. Consequently, the J-V curve became less rectangular and the maximum-power point shifted toward lower output power. This behaviour is directly reflected in the progressive reduction in FF from 77.67 to 76.24, 74.22, 72.21, and 70.19% as series resistance increased from 0 to 1, 2, 3, and 4 Ω.cm^2, respectively. Since the PCE is proportional to the product of V_{OC}, J_{SC}, and FF, and the first two parameters remained constant. The decline in PCE from 11.84 to 10.70% was predominantly caused by the deterioration in FF. The findings show that the series resistance of 0 Ω.cm^2 is the best to ensure high device performance.

3.14 Effect of shunt resistance

Low shunt resistance causes significant power loss in solar cells by offering unwanted leakage pathways for photogenerated current. Such shunting can arise from fabrication defects such as incomplete film coverage, pinholes, edge leakage, conductive filaments, and defective grain-boundary paths. Therefore, higher shunt resistance is required because it suppresses leakage current and improves device performance [45]. The shunt-current contribution is described by Eq.

11, where V is the applied voltage, J_{sh} is the shunt current, and R_{sh} and R_s are the shunt and series resistances, respectively [33].

Figs. 17 & 18b showed that increasing shunt resistance from 100 to 4000 Ω.cm^2 produced a pronounced improvement in the photovoltaic performance of the PSC. At the lowest shunt resistance of 100 Ω.cm^2, the device exhibited V_{OC}, J_{SC}, FF, and PCE of 0.78 V, 19.03 mA/cm^2, 51.11%, and 7.54%. When shunt resistance was increased to 10^3 Ω.cm^2, V_{OC} increased to 0.80 V and FF rose substantially to 75.43%, resulting in a PCE of 11.47%. Further increase in shunt resistance to 2000, 3000, and 4000 Ω.cm^2 progressively increased the FF to 76.84, 77.31, and 77.67%, respectively, while the PCE correspondingly increased to 11.70, 11.78, and 11.84%. In contrast, J_{SC} remained constant at 19.03 mA/cm^2 throughout the investigated range.

The strong deterioration in performance at low shunt resistance could be attributed to increased leakage of photogenerated current through the shunt pathway. When shunt resistance was small, a significant fraction of the generated carriers could flow internally through the low-resistance leakage channel instead of being transported through the external load. This leakage became particularly important in the voltage-producing region of the J-V characteristic and reduced the squareness of the curve (Fig. 18b), resulting in a substantial reduction in FF. The decrease in V_{OC} from 0.80 to 0.78 V at shunt resistance of 100 Ω.cm^2 further indicates that severe shunting can also weaken the maximum photovoltage by facilitating internal current loss. The resulting combination of reduced V_{OC} and, particularly, the severe decline in FF explained the low PCE of 7.54% obtained at the smallest shunt resistance.

$$J_{sh} = \frac{V+JR_s}{R_{sh}}, \qquad 11$$

The constant J_{SC} indicated that shunt resistance did not significantly affect photon absorption or carrier generation, but mainly controlled leakage current. As shunt resistance increased, leakage losses were suppressed, leading to higher FF and PCE, with the improvement becoming small above about 10^3 Ω.cm^2. At shunt resistance of 4000 Ω.cm^2, the device achieved its best performance: V_{OC}, J_{SC}, FF and PCE of 0.80 V, 19.03) mA/cm^2, 77.67%, and 11.84%, respectively. Thus, high shunt resistance is crucial for minimizing leakage and maintaining efficient PSC performance.

3.15 Sensitivity analysis and error margin

Sensitivity and error-margin analyses were performed to quantify the extent to which variations in the investigated physical parameters influence the PCE of the prototype PSC. The error margin represents the relative change between the maximum and minimum PCE obtained over the investigated range of each parameter. On the other hand, sensitivity expresses this variation as a dimensionless fraction [37, 46]. Therefore, parameters with large error margins and sensitivity values exert a stronger influence on device performance and would require tighter control during experimental fabrication. On the other side, parameters with low or negligible sensitivities indicate comparatively greater fabrication tolerance. The error margin and sensitivity were evaluated using Eqs. 12 and 13 [37, 47]. The PCE extrema used for the analysis are summarized in Table 5.

$$\text{Error margin (\%)} = \left(\frac{\Delta PCE}{\text{PCE}_{\text{max}}}\right) \times 100 \qquad 12$$

$$\text{Sensitivity} = \frac{E_m}{100} \qquad 13$$

where $\Delta PCE = \text{PCE}_{\text{max}} - \text{PCE}_{\text{min}}$.

Among all the investigated parameters, the bulk defect density of the Cs_2TiBr_6 absorber exhibited by far the highest sensitivity, with an error margin of 86.23% placing it in the very-high-sensitivity class. The PCE decreases from 11.84% at a defect density of 10^{14} cm^{-3} to only 1.63% at 10^{18} cm^{-3}. This pronounced sensitivity confirm that absorber quality is the most critical factor controlling the photovoltaic performance of the proposed device. The shunt resistance is the next most influential parameter, giving an error margin of 36.32%, corresponding to the high-sensitivity class. Low shunt resistance provided leakage pathways through which photogenerated current could bypass the external circuit, strongly degrading the FF and PCE.

The acceptor carrier concentration of $CuSbS_2$ also showed high sensitivity, with an error margin of 30.02% and sensitivity of 0.300. Increasing its acceptor concentration improved the electrical conductivity of the HTL, strengthened band bending and the built-in electric field at the $Cs_2TiBr_6/CuSbS_2$ heterointerface, and facilitated efficient hole extraction. Similarly, the $Cs_2TiBr_6/CuSbS_2$ interface defect density exhibited high sensitivity, with an error margin of 28.97%. The decrease in PCE with increasing interface defect density indicated the critical role of the absorber/HTL interface in hole extraction and electron blocking. High concentrations of

interface traps enhanced non-radiative recombination, increase the dark saturation current, reduced quasi-Fermi-level splitting, and deteriorate the FF [48, 49]. Therefore, effective passivation of the $Cs_2TiBr_6/CuSbS_2$ interface is another essential requirement for maintaining high device PCE.

Table 5. Error margins and sensitivity of the physical parameters

Parameter varied	Range tested	PCE (%)		Error margin (%)	Sensitivity	Sensitivity class
		Max.	Min.			
Thickness of Cs_2TiBr_6 (μm)	0.6 – 1.4	11.81	10.49	11.18	0.112	Moderate
Thickness of $CuSbS_2$ (μm)	0.2 – 1.2	13.65	11.18	18.10	0.181	Moderate
Thickness of CuI (μm)	0.02 – 0.1	11.86	11.84	0.17	0.002	Negligible
Carrier concentration in the $CuSbS_2$ (cm^{-3})	10^{16} - 10^{19}	11.84	16.92	30.02	0.300	High
Carrier concentration in the CuI (cm^{-3})	1×10^{17} – 9×10^{19}	12.37	11.84	4.28	0.043	Negligible
Defect density of Cs_2TiBr_6 (cm^{-3})	10^{14} - 10^{18}	11.84	1.63	86.23	0.862	Very high
Defect density of $CuSbS_2$ (cm^{-3})	10^{14} - 10^{17}	11.84	11.19	5.49	0.055	Low
Defect density of CuI (cm^{-3})	10^{14} - 10^{18}	11.84	11.84	0.00	0.00	Negligible
Electron capture cross section in Cs_2TiBr_6 (cm^{-3})	10^{-15} - 10^{-19}	12.33	11.84	3.97	0.040	Negligible
Interface defect density of $Cs_2TiBr_6/CuSbS_2$ (cm^{-2})	10^{10} - 10^{15}	12.29	8.73	28.97	0.290	High
Interface defect density of $CuSbS_2$/CuI (cm^{-2})	10^{10} - 10^{15}	12.17	10.02	17.67	0.177	Moderate
Series resistance (Ωcm^2)	0 - 4	11.84	10.70	9.63	0.096	Low
Shunt resistance (Ωcm^2)	100 - 4000	11.84	7.54	0.363	0.363	High

Moderate sensitivity is obtained for the $CuSbS_2$ thickness, $CuSbS_2$/CuI interface defect density, and Cs_2TiBr_6 absorber thickness. These parameters exhibited appreciable effects on performance but were less critical than absorber defect density, shunt resistance, $CuSbS_2$ doping,

and the absorber/HTL interface quality. Absorber thickness represented a compromise between enhanced photon absorption and increased carrier-transport and recombination losses, whereas $CuSbS_2$ thickness influenced rear-contact selectivity and hole extraction. The $CuSbS_2$/CuI interface defect density affected charge transfer and recombination within the bilayer HTL, explaining its moderate sensitivity. The series resistance and $CuSbS_2$ defect density exhibit relatively low sensitivities. Increasing effect of series resistance could principally be associated with the progressive reduction in FF, while V_{OC} and J_{SC} remained unchanged. The low sensitivity to $CuSbS_2$ bulk defects similarly indicates that moderate variations in HTL defect density could be tolerated because the principal photogeneration and quasi-Fermi-level splitting occur predominantly within the Cs_2TiBr_6 absorber.

In contrast, CuI thickness, CuI acceptor carrier concentration, CuI defect density, and the absorber electron capture cross-section fell within the negligible-sensitivity class. This confirmed that once a sufficiently thin, continuous, and conductive CuI layer was established, moderate changes in its physical properties had little influence on the device performance. The relatively weak dependence also emerged because CuI was positioned behind the $CuSbS_2$ layer and functioned principally as a secondary hole-selective transport layer rather than as the primary photon absorber.

3.16 Photovoltaic performance of the optimized cell

The optimal parameters for simulating the final device are presented in Table 6. The Series resistance is taken for an ideal value of 0 Ωcm^2, while the shunt resistance is kept at a realistic value of 4000 Ωcm^2 [50, 51]. To ensure defensible and practically realistic parameters, the optimal values were chosen to agree with experimental carrier concertation for $CuSbS_2$ [52, 53], CuI [54, 55], minimum bulk defects density of 10^{14} cm^{-3} [56, 57], interface defects density of 10^{10} cm^{-3} [58, 59]. Also, HTL thickness of 20 nm [60, 61] and 1200 nm [62]. Also, absorber thickness 1400 nm has been reported for experimental fabricated PSCs [63, 64].

Table 6. Optimal parameters obtained for simulation of the optimized cells.

Optimal parameters	Cs_2TiBr_6	$CuSbS_2$	CuI
Thickness (μm)	1.4	1.2	0.02
N_D (cm^{-3})	-	0	-
N_A (cm^{-3})	-	10^{19}	9×10^{17}
Bulk defect density, N_t (cm^{-3})	10^{14}	10^{14}	10^{14}
All interface defect, N_t (cm^{-2})			10^{10}
Electron capture cross section for electrons in the absorber layer (cm^2)			10^{-19}

The remarkable improvement in the photovoltaic performance of the optimized FTO/Cs_2TiBr_6/$CuSbS_2$/CuI/Au PSC come from the combined optimization of optical absorption, carrier transport, interface quality, and recombination dynamics (Table 6). The optimized device achieved a V_{OC}, J_{SC}, FF and PCE of 1.26 V, 23.57 mA/cm^2, 89.12%, and an excellent PCE of 26.49% (Table 7, Fig. 19), representing a substantial improvement over the prototype cell.

The increase in absorber thickness to 1.4 µm improved light absorption by extending the optical path length within the Cs_2TiBr_6 absorber layer. This allowed more photons, especially those close to the absorption edge, to be harvested and converted into electron-hole pairs. Simultaneously, the optimized $CuSbS_2$ thickness of 1.2 µm provided a highly effective hole-selective contact to ensure efficient extraction of photogenerated holes while suppressing electron leakage toward the rear electrode. The thin 0.02 µm CuI layer served as an efficient secondary hole-transport layer that established a cascade-like valence-band alignment with $CuSbS_2$, facilitated rapid hole transport to the Au contact and maintained excellent electron-blocking capability. This graded band alignment minimized carrier accumulation at the HTL interfaces and significantly reduced recombination losses.

Table 7. Photovoltaic performance of the optimized PSCs using Au and Carbon back contacts.

Optimized Cell	V_{OC} (V)	J_{SC} (mA/cm^2)	FF (%)	PCE (%)
FTO/Cs_2TiBr_6/$CuSbS_2$/CuI/Au	1.26	23.57	89.12	26.49
FTO/Cs_2TiBr_6/$CuSbS_2$/CuI/C	1.26	23.57	89.11	26.49

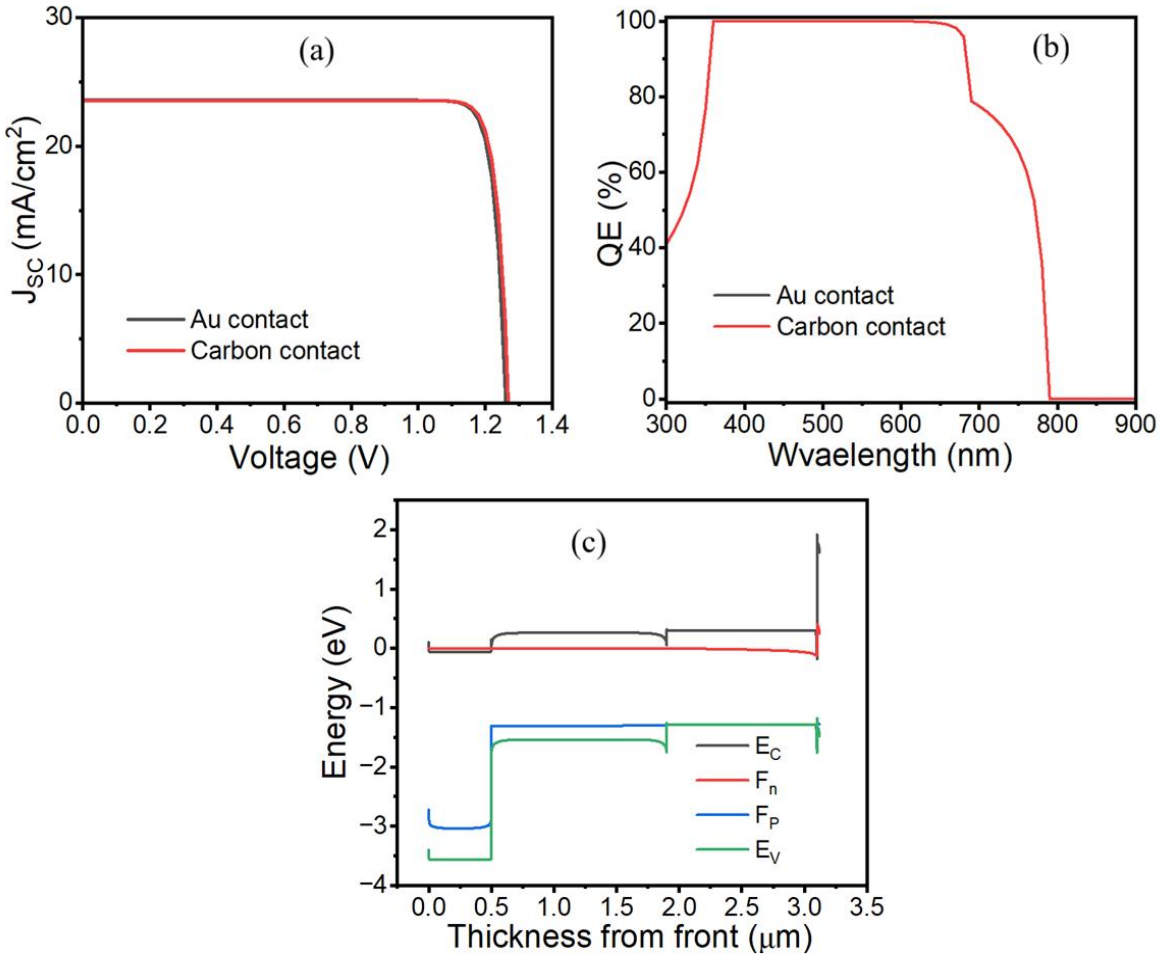


Figure 19. J-V characteristic of the optimized ETL-free PSCs employing Au and C back contact, (b) Associated QE spectra, (c) Energy band diagram of the cell employing C rear contact.

The optimal acceptor concentrations further improved the electrical properties of the bilayer HTL. The substantially doped $CuSbS_2$ (10^{19} cm^{-3}) exhibited high electrical conductivity, stronger band bending, and an enhanced built-in electric field at the $Cs_2TiBr_6/CuSbS_2$ interface, promoted rapid hole extraction and reduced charge accumulation [65]. Likewise, the optimized CuI acceptor concentration ensured improved hole transport toward the Au electrode while maintaining excellent contact selectivity. Together, these optimized HTLs reduced series transport losses and preserved efficient carrier collection throughout the device.

Defect engineering also contributed significantly to the excellent device performance. The moderate $CuSbS_2$ bulk defect density minimized trap-assisted Shockley-Read-Hall recombination within the HTL, while the optimal value of interface defect density effectively suppressed non-radiative recombination at all heterointerfaces [66]. Furthermore, reducing the electron capture cross-section in the Cs_2TiBr_6 absorber to decreased the probability of electron trapping by deep defect states, thereby extending the minority-carrier lifetime and increasing carrier diffusion length. The idealized optimal series resistance of 0 $\Omega.cm^2$ further eliminated resistive voltage losses and allowed efficient carrier transport from the absorber to the external circuit.

The exceptionally high V_{OC} (1.26 V) reflect the substantial suppression of non-radiative recombination and the preservation of a large quasi-Fermi-level splitting under illumination [67]. The enhanced JSC (23.57 mA/cm^2) demonstrates that the optimized architecture combines efficient photon absorption with highly effective carrier collection. More importantly, the FF of 89.12% indicates excellent diode quality, minimal resistive loss, and highly selective carrier transport across the heterojunctions. Collectively, these improvements confirm that the optimized bilayer HTL configuration successfully balanced optical absorption, carrier extraction, transport, and recombination control.

The optimized PCE of 26.49% is remarkably close to the Shockley-Queisser limit of 26.86% for a 1.8 eV single-junction absorber, corresponding to ~98.6% of the theoretical maximum PCE. This close agreement suggest that the optimized device operated near the detailed-balance limit under the assumptions of the SCAPS-1D model. The remaining PCE gap of only 0.37% points could be associated with unavoidable radiative losses and the residual non-radiative recombination incorporated into the simulation. Therefore, the optimized device architecture demonstrates that careful optimization of layer thicknesses, HTL doping, defect passivation, interface quality, and

carrier-capture probability can drive ETL-free lead-free PSCs toward their theoretical performance limit.

The enhancement of the QE in the wavelength range of 450 to ~890 nm supports the improve J_{SC} due to increased photon absorption, carrier generation and extraction [65, 68].

3.16.1 Photovoltaic performance of the optimized cell using economically viable carbon back contact

Investigating the effect of the rear contact is essential because it determines energy-level alignment, hole extraction, contact resistance, and the long-term operational stability of perovskite solar cells [69]. Although Au is the most widely used back electrode because of its high conductivity, suitable work function, and excellent chemical stability, its high-cost limits large-scale commercialization [70, 71]. Carbon has therefore emerged as a promising alternative due to its low-cost, earth-abundant, chemically inert, hydrophobic, and compatible with scalable, vacuum-free fabrication techniques such as screen printing, blade coating, and roll-to-roll processing [72]. Therefore, comparing optimized Au- and carbon-contact devices can provide valuable insight into whether a low-cost carbon electrode can maintain the photovoltaic performance of conventional Au-contact PSCs while significantly reducing fabrication cost and improving commercial viability [73, 74].

The alternative FTO/Cs_2TiBr_6/$CuSbS_2$/CuI/C PSC exhibited an equivalent/identical photovoltaic performance with the Au contact-based device (Table 7, Fig. 19). The negligible difference in FF (0.01%) confirmed that replacing Au with carbon introduced virtually no additional electrical loss under the optimized device conditions.

The comparable photovoltaic performance obtained with Au and carbon back contacts can be attributed to the favorable energy-level alignment established by the optimized $CuSbS_2$/CuI bilayer HTL. Carbon, with a work function of approximately 5.0 eV, is well matched to the valence-band edge of the outer CuI layer, enabling efficient hole collection while maintaining sufficient selectivity against electron back injection. Because the $CuSbS_2$/CuI bilayer already provided efficient hole transport and suppressed minority-carrier leakage, the rear electrode primarily acted as a hole-collecting contact. Consequently, replacing Au with carbon produced

negligible changes in the built-in electric field, band bending, carrier selectivity, and quasi-Fermi-level splitting, thereby preserving the device performance.

Figure 19c shows the equilibrium energy-band diagram of the optimized FTO/Cs_2TiBr_6/$CuSbS_2$/CuI/C solar cell. The device exhibited a favorable cascade-like band alignment that facilitated charge separation and selective carrier transport. At the FTO/Cs_2TiBr_6 interface, a small conduction-band offset (CBO) of ~ +0.10 eV promoted electron extraction while limiting interfacial recombination. At the Cs_2TiBr_6/$CuSbS_2$ interface, a valence-band offset (VBO) of ~ +0.16 eV provided a favorable pathway for hole transfer from the absorber into the HTL. The subsequent $CuSbS_2$/CuI interface exhibited a similarly small VBO of about +0.10 eV, further promoting hole transport through the bilayer. On the other hand, the comparatively large conduction-band barriers within the HTL stack suppressed electron leakage toward the rear contact. The carbon electrode therefore formed an effectively ohmic or near-ohmic contact with CuI, allowing efficient hole collection with minimal additional contact losses.

Replacing C for Au maintained the device electrostatics and carrier-transfer properties, producing identical photovoltaic metrics: V_{OC}, J_{SC}, FF, and PCE of 1.26 V, 23.57 mA/cm^2, 89.11%, and 26.49%, respectively. This attribute emerged from the favorable $CuSbS_2$/CuI band alignment and low interface defect densities, which mitigated non-radiative recombination and facilitated efficient carrier extraction. The nearly overlapping J-V curves (Fig. 19a) confirm that both contacts provided similar diode behavior, recombination losses, and series resistance, indicating that charge transport was controlled mainly by the optimized Cs_2TiBr_6/$CuSbS_2$/CuI heterostructure. Likewise, the identical QE spectra (Fig. 19b) showed that replacing Au with C did not significantly affect photon absorption, carrier generation, or collection, consistent with the identical J_{SC}.

3.16.2 Carrier generation and recombination rate for the optimized devices employing Au and C back contact

Fig. 20a illustrates the spatial distribution of the photogenerated carrier generation rate for the optimized FTO/Cs_2TiBr_6/$CuSbS_2$/CuI/Au and FTO/Cs_2TiBr_6/$CuSbS_2$/CuI/C PSCs. The generation profiles of both solar cells are identical throughout the device thickness. This suggested that replacing Au with carbon had no measurable influence on optical absorption or photocarrier generation. The generation rate rose sharply (0.5 μm in the Cs_2TiBr_6 absorber) to a maximum value

of 6.0 × 10^{21} $cm^{-3}s^{-1}$, after which it decreased exponentially with increasing depth through the absorber. This behaviour followed the Beer-Lambert absorption law, where the incident photon flux decreased as light penetrated deeper into the semiconductor because photons were progressively absorbed to generate electron-hole pairs. As a result, carrier generation was highest near the illuminated FTO/Cs_2TiBr_6 interface and gradually diminished toward the rear contact due to the reduced photon population available for absorption.

A second, smaller generation peak of 1.27 × 10^{21} $cm^{-3}s^{-1}$ appeared on the surface of the $CuSbS_2$ layer (1.9 µm). This feature originated from the change in optical field distribution at the heterointerfaces and the finite optical absorption within the HTLs. The identical generation profiles explained why both optimized devices exhibited the same J_{SC} (23.57 mA/cm^2) and identical QE spectra (Fig. 19). The findings demonstrated that the back-contact material did not influence photon harvesting once efficient carrier-selective transport layers remained the same.

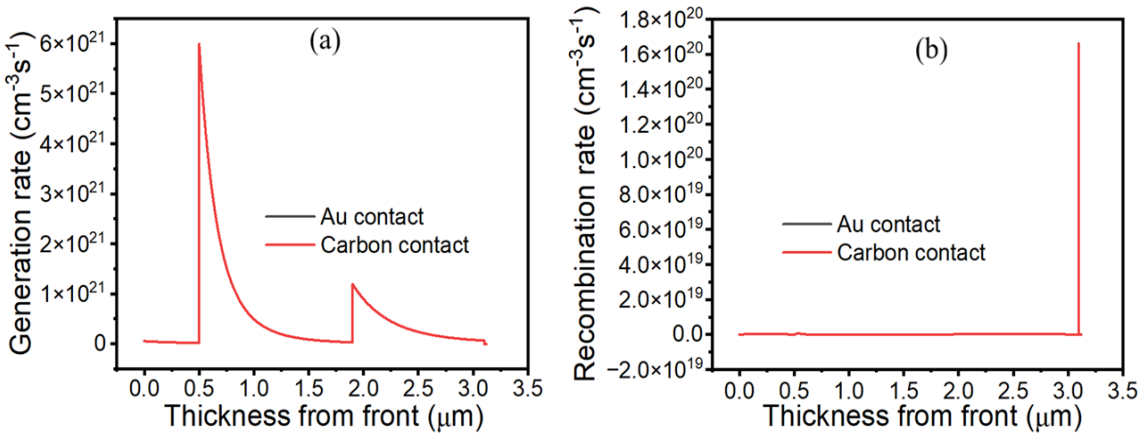


Figure 20. (a) Carrier generation rates for the cells emplouing Au and C back contact, (b) Carrier recombination rates.

Fig. 20b depicted the corresponding carrier recombination-rate profiles. For both devices, the recombination rate remained extremely low throughout the absorber and transport layers, and over most of the device thickness. Only at the extreme rear contact (CuI/Au or C) did the recombination rate increased abruptly to approximately 4.75 × 10^{20} $cm^{-3}s^{-1}$ (at 3.1 µm). This localized increase was expected because the metallic back electrode represented the terminal carrier collection region where the remaining minority carriers are removed or recombine after

charge extraction. The absence of significant recombination within the bulk Cs_2TiBr_6 absorber confirmed that the optimized bulk defect density (10^{14} cm^{-3}), interface defect density (10^{10} cm^{-2}), and reduced electron capture cross-section (10^{-19} cm^2) effectively suppressed Shockley-Read-Hall recombination throughout the active region of the device.

The complete overlap of the recombination curves for the Au- and C-contact devices further demonstrated that replacing Au with carbon did not introduce additional recombination centres or increase contact-related carrier losses. Instead, the optimized $CuSbS_2$/CuI bilayer provided highly efficient hole extraction while simultaneously blocking electron leakage toward the rear contact. This there assisted to maintain nearly identical recombination dynamics irrespective of the electrode material.

3.16.3 Comparison of the current finding with related works on Cs_2TiBr_6-based PSCs.

To provide a meaningful comparison for the optimized device, the present benchmarking is restricted to previously reported Cs_2TiBr_6-based PSCs with PCEs exceeding 20%. The high-efficiency devices identified within this range are predominantly numerical predictions. Their performance should therefore be compared with consideration of differences in device architecture, transport materials, defect assumptions, contact properties, and optimization conditions.

Table 8. Summary of the Cs_2TiBr_6-based PSCs in comparison with the present work

PSC architecture	PCE (%)	Reference
FTO/Cs_2TiBr_6/$CuSbS_2$/CuI/Au or C	26.49	Present work
ETL-free		
Al/FTO/ZnSe/Cs_2TiBr_6/V_2O_5/Os	31.02	[75]
FTO/CeO_x/Cs_2TiBr_6/Cu_2O/CuO/Pt	30.75	[27]
FTO/IZGO/Cs_2TiBr_6/$CuSbS_2$/Se	29.19	[76]
FTO/LBSO/Cs_2TiBr_6/$CuSbS_2$/Au	29.13	[77]
FTO/Cs_2TiBr_6/CZTS/NiO/Au, ETL-free	27.78	[26]
FTO/ZnO/Cs_2TiBr_6/$CuSbS_2$/Pt	26.96	[15]
ITO/LBSO Cs_2TiBr_6/CNTS/Au	24.82	[17]
FTO/SnO_2/Cs_2TiBr_6/CBTS/Au	24.24	[12]
TCO/CdS/Cs_2TiBr_6/$CuSbS_2$/Au	23.77	[11]
FTO/CeO_x/Cs_2TiBr_6/CZTS/P3HT/C	22.61	[9]

FTO/SnO_2/Cs_2TiBr_6/MoO_x/Au	20.11	[78]

The PCE of 26.49% achieved in the present work exceeds several previously reported high-performance Cs_2TiBr_6 architectures [9, 11, 12, 17, 78] (Table 8). It is also highly competitive with the 26.96% reported by Karmaker et al. [15], differing by only 0.47% points. Importantly, the present device simultaneously achieves a high V_{OC} of 1.26 V and FF of ~89.1%, indicating a balanced optimization of voltage generation, charge extraction, and recombination suppression.

Higher simulated PCEs have nevertheless been reported [27, 36, 75-77] (Table 8). These superior results demonstrate that the present 26.49% should not be regarded as the highest simulated PCE reported for Cs_2TiBr_6. Rather, its significance lies in achieving a competitive efficiency using a simplified ETL-free architecture and a $CuSbS_2$/CuI novel bilayer HTL, while also permitting replacement of the conventional Au contact with a low-cost carbon without any loss in photovoltaic performance.

The advantage of the present C-contact device is particularly evident when compared with the 22.61% C-contact Cs_2TiBr_6-based device reported by Lin et al [9]. The proposed FTO/Cs_2TiBr_6/$CuSbS_2$/CuI/C structure improved the simulated PCE by 3.88% points, while eliminating the ETL and retained the same 26.49% PCE obtained with Au. In contrast, several of the higher-efficiency literature devices employ additional electron-transport layers and/or relatively costly rear electrodes such as Au, Pt, or Os.

3.16.4 Effect of temperature on optimized cells utilizing Au and C rear contacts

Investigating the effect of operating temperature is essential because photovoltaic PSCs experience continuous temperature fluctuations under outdoor conditions, which affect the semiconductor bandgap (Eq. 14), intrinsic carrier concentration (Eq. 15), carrier mobility, recombination kinetics, and contact properties [79-82] These temperature-dependent changes influence the performance metrics, and long-term operational stability of PSCs. Therefore, evaluating device performance over a practical temperature range offers valuable insight into the thermal robustness, reliability, and suitability of the proposed configuration for real-world photovoltaic applications [80, 81].

$$E_g(T) = E_g(0) - \frac{\alpha T^3}{T + \beta} \qquad 14$$

$$n_i(T) = \sqrt{N_C N_V}\exp(\frac{E_g(T)}{2k_B T}) \quad 15$$

where $E_g(0)$ is the bandgap at 0 K, T is absolute temperature, and α and β are material-dependent parameters, N_C and N_V are the effective densities of states, and k_B is the Boltzmann constant.

An increase in temperature from 290 to 330 K showed the same performance trend in both device (using Au and C contacts). V_{OC} decreased from 1.27 to 1.23 V, FF decreased slightly from about 89.24 to 88.65%, and PCE declined from 26.70 to 25.73%. In contrast, J_{SC} increased slightly from approximately 23.56 to 23.66 mA/cm^2 [Fig. 21a]. This indicated that the temperature response was controlled by voltage and recombination losses rather than photocurrent generation.

The reduction in V_{OC} with increasing temperature was the dominant reason for the decline in PCE. At higher temperature, the intrinsic carrier concentration increased and the bandgap of the Cs_2TiBr_6 absorber slightly narrowed. These effects increased the reverse saturation current and strengthened thermally activated Shockley-Read-Hall recombination. Since V_{OC} depends logarithmically on the ratio between photocurrent and saturation current, an increase in recombination current directly reduced the quasi-Fermi level splitting, resulting in lower V_{OC} [83]. This explained the steady decrease from 1.27 V at 290 K to 1.23 V at 330 K.

The slight increase in J_{SC} with temperature was attributed to bandgap narrowing, which allowed the absorber to harvest a slightly broader portion of the solar spectrum [67]. As the optical absorption edge shifted toward longer wavelengths, additional low-energy photons contributed to carrier generation. However, this increase was very small because the bandgap shift over the investigated temperature range was limited. Therefore, the gain in J_{SC} was insufficient to compensate for the voltage loss.

The decrease in FF was associated with enhanced recombination and increased carrier thermalization losses at higher temperature. Thermally activated defects became more active, carrier scattering increased, and the diode ideality worsened slightly. These effects reduced the squareness of the J-V curve and caused the FF to decline from 89.20 to 88.65%.

Both Au- and C-contact devices showed almost identical temperature-dependent behaviour, indicating that the rear contact did not control the thermal stability of the optimized

cells. The very close performance of the C-contact device to the Au-contact device confirmed that C can serve as an efficient and thermally stable rear electrode without introducing additional temperature-dependent transport losses. The optimized devices maintained high PCEs above 25.7% even at 330 K, showcasing good thermal robustness of the proposed ETL-free Cs_2TiBr_6/$CuSbS_2$/CuI architecture.

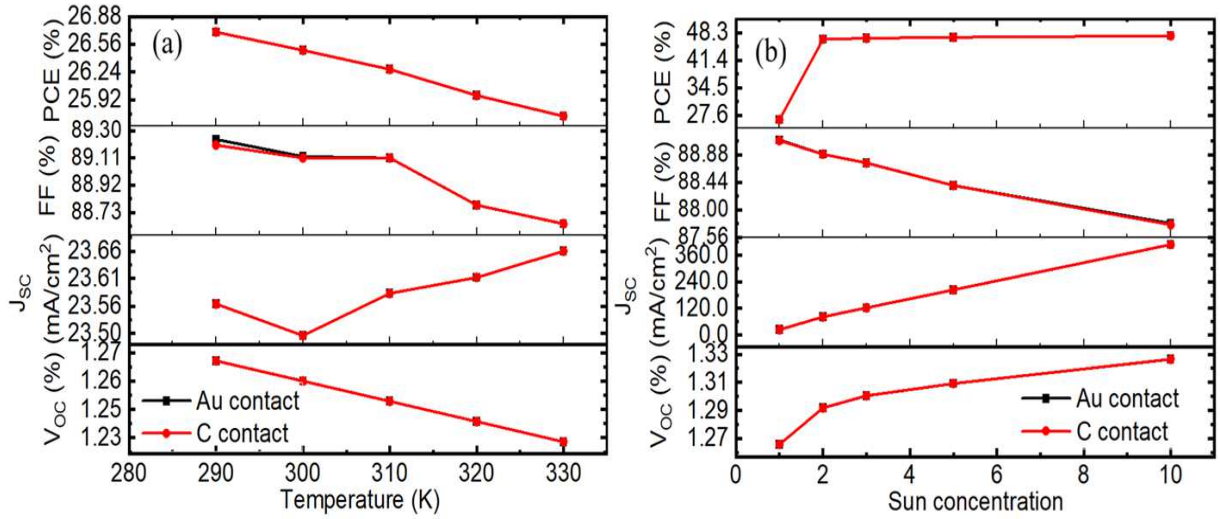


Figure 21. Dependence of V_{OC}, J_{SC}, FF and PCE on (a) temperature, (c) Sun concentration.

3.16.5 Effect of sun concentration

Evaluating the effect of solar concentration is important because increasing the incident photon flux drives the device into progressively substantial carrier-injection regimes, thereby modifying photogeneration, quasi-Fermi-level splitting, recombination kinetics, charge transfer, and resistive losses. Under a concentration factor C, the photogeneration rate and, under efficient extraction, the J_{SC} are expected to increase approximately linearly with photon flux, $G(C) \approx CG_{1sun}$ and $J_{SC}(C) \approx CJ_{SC,1sun}$. The resulting increase in steady-state electron and hole populations widens the quasi-Fermi-level splitting and therefore increases V_{OC} logarithmically with illumination intensity. However, at sufficiently high carrier densities, bimolecular radiative and other injection-dependent recombination processes (Eq. 16) become increasingly paramount, while the larger photocurrent amplifies ohmic losses through the series resistance and electrical contacts (Eq. 17). As a result, the evolution of V_{OC}, J_{SC}, FF, and PCE with concentration offers a sensitive probe of absorber

quality, interfacial recombination, carrier-selective transport, and contact resistance. It also helps in assessing the suitability of the device architecture for concentrator photovoltaic operation. Experimental perovskite cells have shown increased PCE under moderate concentration, together with concentration-dependent recombination and stability effects [84].

$$R = R_{SRH} = Bnp + C_n n^2 p + C_p n p^2 \quad (16)$$

$$P_{loss,R_s} = J^2 R_s \quad (17)$$

where R_{SRH} denotes trap-assisted recombination, Bnp designate bimolecular radiative recombination, and the last terms represent Auger recombination. As concentration increases, n and p rise. Therefore, the higher-order recombination channels become increasingly important. Experimental light-intensity measurements in PSCs have likewise demonstrated that the balance between trap-assisted and bimolecular recombination changes with carrier density [84].

Fig. 21b showed that both rear contacts (Au and C) respond almost identically under concentrated illumination. As the sun concentration increased from 1 to 10 suns, the J_{SC} increased significantly from about 23.57 to 408.3 mA/cm^2, while V_{OC} increased moderately from 1.26 to 1.33 V. The FF decreased slightly from about 89.12 to 87.78%, but the PCE increased from 26.49% to about 47.5%. This indicated that the devices benefit significantly from enhanced photogeneration under concentrated light, while still maintaining good diode quality and low recombination losses. The substantial increase in J_{SC} was expected because photocurrent is directly proportional to the generation rate of electron-hole pairs. Under higher illumination intensity, more photons were absorbed in the Cs_2TiBr_6 absorber, producing more free carriers and increasing the current density. Therefore, the rise in J_{SC} with sun concentration reflected enhanced optical generation.

The increase in V_{OC} with solar concentration arose from the higher photogenerated carrier density, which widened the quasi-Fermi-level splitting. Because V_{OC} depends logarithmically on light intensity, it increased only modestly from 1.26 to 1.33 V despite the much larger rise in J_{SC}. The slight reduction in FF from 89.1% to 87.8% was attributed to increased recombination and current-dependent resistive losses at high carrier densities. Higher illumination enhanced bimolecular and trap-assisted recombination, while the larger current magnified residual series-resistance losses near the maximum-power point. The identical response of the Au- and C-contact

devices indicated that the rear contact did not limit performance under concentrated illumination. The optimized $CuSbS_2$/CuI bilayer maintained efficient hole extraction and electron blocking for both contacts, confirming carbon as a low-cost alternative to Au without sacrificing device performance.

3.16.6 Practical Implications and Modeling Limitations

The present results provide useful design guidelines for the experimental development of efficient lead-free Cs_2TiBr_6-based PSCs. In particular, elimination of the ETL reduces the number of functional layers and heterointerfaces, which could simplify device production and reduce material consumption and fabrication cost. The ability of the optimized $CuSbS_2$/CuI bilayer to maintain a simulated PCE of 26.49% with either Au or carbon further indicates that expensive noble-metal rear contacts may not be essential when appropriate hole-selective layers are deployed. Carbon is specifically attractive for practical implementation because of its low cost, abundance, chemical robustness, and compatibility with scalable vacuum-free deposition techniques, such as screen printing and blade coating.

The sensitivity analysis also identifies the material properties that should receive the greatest experimental attention. The strong dependence of device efficiency on Cs_2TiBr_6 bulk defect density demonstrates that high-quality absorber films with low concentrations of recombination-active defects are essential. Similarly, the pronounced sensitivity to the Cs_2TiBr_6/$CuSbS_2$ interface defect density and $CuSbS_2$ acceptor concentration highlights the importance of interface passivation, controlled HTL doping, and favorable energy-level alignment. In contrast, the relatively weak sensitivity to CuI thickness and bulk defect density indicates a wider processing tolerance for the outer CuI layer once a thin, continuous, and sufficiently conductive film is obtained. These findings therefore provide a useful hierarchy of parameters for guiding experimental optimization.

However, the predicted 26.49% PCE should be interpreted as an upper-bound theoretical performance under optimized SCAPS-1D conditions rather than an immediately achievable experimental efficiency. The simulation treats the device as a one-dimensional structure with laterally uniform layers and well-defined material parameters. Real devices may contain thickness

variations, pinholes, grain boundaries, surface roughness, compositional fluctuations, incomplete film coverage, and spatially non-uniform defect distributions that are not explicitly represented in the model [85]. Such imperfections can introduce additional recombination and resistive losses.

Several optimized input parameters are also highly favorable. For example, the model combines a low interface defect density of 10^{10} cm^{-2}, low bulk defect densities, a very small electron capture cross-section, high HTL carrier concentrations, a high shunt resistance, and an ideal series resistance of 0 Ωcm^2. Although individual values within these ranges have experimental precedent, achieving all of them simultaneously in a single Cs_2TiBr_6/$CuSbS_2$/CuI device may be challenging. The model also assumes fixed material properties and does not explicitly describe dynamic phenomena such as ion migration, field-induced redistribution of charged defects, current-voltage hysteresis, interfacial chemical reactions, electrode diffusion, or progressive material degradation during prolonged illumination and thermal cycling [86, 87].

Another consideration concerns the optical contribution of the relatively thick $CuSbS_2$ layer. The optimized $CuSbS_2$ thickness is 1.2 μm and its bandgap is lower than that of Cs_2TiBr_6; consequently, $CuSbS_2$ may contribute additional photon absorption and carrier generation rather than functioning exclusively as a passive HTL.

Furthermore, the equivalent performance predicted for Au and carbon assumes favorable CuI/contact energetics and does not fully capture differences in real contact morphology, contact resistivity, carbon-paste composition, interfacial reactions, or long-term contact degradation [88]. Experimental carbon electrodes may also exhibit greater sheet and contact resistance than evaporated Au, particularly when devices are scaled to larger areas [89, 90]. Therefore, the simulated equivalence of Au and carbon establishes the electronic feasibility of carbon substitution but requires experimental confirmation under realistic fabrication conditions.

4. Conclusion

This study demonstrates a high-performance device-design strategy for electron-transport-layer-free, Pb-free Cs_2TiBr_6 PSCs via systematic SCAPS-1D optimization of the FTO/Cs_2TiBr_6/$CuSbS_2$/CuI configuration. Among the prototype configurations, the $CuSbS_2$/CuI bilayer HTL delivered the best starting performance, confirming the benefit of combining

favorable hole extraction at the $Cs_2TiBr_6/CuSbS_2$ interface with efficient hole transport and electron blocking through CuI. Device performance was governed most strongly by Cs_2TiBr_6 bulk defect density, shunt resistance, $CuSbS_2$ acceptor concentration, and the $Cs_2TiBr_6/CuSbS_2$ interface quality, identifying absorber quality and interfacial control as the principal experimental priorities. After simultaneous optimization of layer thicknesses, carrier concentrations, defect densities, capture cross-section, and resistive parameters, the Au-contact device achieved a V_{OC}, J_{SC}, FF, and PCE of 1.26 V, 23.57 mA/cm^2, 89.12%, and 26.49%, respectively, compared with 11.84% for the prototype. Remarkably, replacing Au with carbon preserved the same 26.49% PCE and nearly identical FF of 89.11%, demonstrating the electronic feasibility of a substantially lower-cost rear contact. Both optimized devices also exhibited relatively the same responses to temperature and concentrated illumination, indicating that the optimized heterostructure, rather than the electrode material, primarily controls performance. The sensitivity trends provide fabrication targets for prioritizing absorber passivation, controlled HTL doping, and low-loss carbon-contact integration during experimental translation. Nevertheless, the predicted efficiency represents an optimized theoretical limit. Experimental fabrication is required to validate the assumed defect control, interface quality, contact resistance, morphology, and long-term operational stability.

Acknowledgements

The authors would like to appreciate the UKRI Ayrton Challenge Fund - UKRI319: REACH-PSM: Resilient Renewable Energy Access Through Community-Driven Holistic Development in Perovskite Solar Module Manufacturing.

Author Contributions

I.A.T.: Conceptualization, Investigation, Writing – original draft; **P.R.J.:** Conceptualization, Investigation, Writing – original draft; **V.M.I.:** Conceptualization, Simulation; **O.D.A.:** Conceptualization, Simulation; **A,N.A:** Method, Writing – review & editing; **O.M.E.:** Investigation, Writing – review & editing; **M.O.B.:** Software; **F.A.:** Validation; **K.V.K**.: Validation, Writing – review & editing; **D.D.H.:** Software; **J.N.T.:** Software.

Declarations

Ethical Approval

This declaration is not applicable.

Consent to Publish Declaration

Not applicable

Consent to Participate Declaration

Not applicable

Clinical Trial Registration

Not applicable

Competing interests

The authors state that they have no known competing financial interests or personal relationships that could have appeared to influence the work reported in this paper.

Funding

The authors have declared the source of fund received for this research work in the Acknowledgment section of this work.

Data Availability

The data for this work will be made available on request.

Reference

1. Najmul Hoque, S.M.; Das, B.K. Present status of solar home and photovoltaic micro utility systems in Bangladesh and recommendation for further expansion and upgrading for rural electrification. *Journal of Renewable and Sustainable Energy* 5 (2013) 043123. DOI: 10.1063/1.4812993.

2. Kumar, M.; Raj, A.; Kumar, A.; Anshul, A. Computational analysis of bandgap tuning, admittance and impedance spectroscopy measurements in lead-free $MASnI_3$ perovskite solar cell device. *International Journal of Energy Research* 46 (2022) 11456–11469. DOI: 10.1002/er.7942.

3. Kojima, A.; Teshima, K.; Shirai, Y.; Miyasaka, T. Organometal halide perovskites as visible-light sensitizers for photovoltaic cells. *Journal of the American Chemical Society* 131 (2009) 6050–6051. DOI: 10.1021/ja809598r.

4. Kim, H.-S.; Lee, C.-R.; Im, J.-H.; et al. Lead iodide perovskite sensitized all-solid-state submicron thin-film mesoscopic solar cell with efficiency exceeding 9%. *Scientific Reports* 2 (2012) 591. DOI: 10.1038/srep00591.

5. National Renewable Energy Laboratory (NREL). *Best Research-Cell Efficiency Chart*. National Renewable Energy Laboratory, Golden, Colorado, USA, updated 2025.

6. Xu, D.; Xiao, K.; Liu, Y.; et al. Lead carboxylates passivation for meter-scale perovskite solar modules. *Nature* (2026). DOI: 10.1038/s41586-026-10994-7.

7. Chen, M.; Ju, M.-G.; Carl, A.D.; Zong, Y.; Grimm, R.L.; Gu, J.; Zeng, X.C.; Zhou, Y.; Padture, N.P. Cesium titanium (IV) bromide thin films based stable lead-free perovskite solar cells. *Joule* 2 (2018) 558–570. DOI: 10.1016/j.joule.2018.01.009.

8. Li, X.; Shi, J.; Chen, J.; Tan, Z.; Lei, H. Lead-free halide double perovskites for high-performance photodetectors: Progress and perspective. *Materials* 16 (2023) 4490. DOI: 10.3390/ma16124490.

9. Lin, W.; Chen, X.; Ji, Z.; Gao, W.; Zhao, N.; Li, M.; Zhang, D.; Ling, Y.; Wu, J.; Huang, K.; Yu, J. Optimization of Cs_2TiBr_6-based perovskite solar cells with double hole transport layer by SCAPS-1D simulation. *Materials Today Communications* 46 (2025) 112841. DOI: 10.1016/j.mtcomm.2025.112841.

10. Zhang, F.; Cocchi, C.; Draxl, C. Giant excitonic effects in vacancy-ordered double perovskites. *Physical Review B* 107 (2023) 235119. DOI: 10.1103/PhysRevB.107.235119.

11. Mercy, P.A.M.; Wilson, K.S.J. Development of environmental friendly high performance Cs_2TiBr_6 based perovskite solar cell using numerical simulation. *Applied Surface Science Advances* 15 (2023) 100394. DOI: 10.1016/j.apsadv.2023.100394.

12. Gupta, S.; Kaur, J.; Basu, R.; Sharma, A.K.; Pandey, R.; Madan, J. Lead-free Cs_2TiBr_6 perovskite solar cells achieving high power conversion efficiency through device simulation. *Micro and Nanostructures* 196 (2024) 207991. DOI: 10.1016/j.micrna.2024.207991.

13. Saha, P.; Halder, P.; Singh, S.; Bhattacharya, S. Optimization and formulation of different hole-transporting materials (HTMs) for the performance of eco-friendly Cs_2TiBr_6-based perovskite solar cells. *Energy Technology* 12 (2024) 2300991. DOI: 10.1002/ente.202300991.

14. You, L.; Zhang, X.; Ma, Q.; Zhu, W.; Wu, J. Optimization of electron transport layer-free Cs_2TiBr_6/$MASnBr_3$ laminated structure perovskite solar cells by SCAPS-1D simulation. *Physica Status Solidi A* 220 (2023) 2300071. DOI: 10.1002/pssa.202300071.

15. Karmaker, H.; Siddique, A.; Das, B.K. Numerical investigation of lead-free Cs_2TiBr_6-based perovskite solar cell with optimal selection of electron and hole transport layer through SCAPS-1D simulation. *Results in Optics* 13 (2023) 100571. DOI: 10.1016/j.rio.2023.100571.

16. Urmi, S.S.; Khan, M.A.K.; Ferdous, T.T.; Adinehloo, D.; Perebeinos, V.; Alim, M.A. Cs_2TiI_6 ($Cs_2TiI_xBr_{6-x}$) halide perovskite solar cell and its point defect analysis. *Nanomaterials* 13 (2023) 2100. DOI: 10.3390/nano13142100.

17. Hossain, M.K.; Islam, S.; Sakib, M.N.; et al. Exploring the optoelectronic and photovoltaic characteristics of lead-free Cs_2TiBr_6 double perovskite solar cells: A DFT and SCAPS-1D investigation. *Advanced Electronic Materials* 11 (2025). DOI: 10.1002/aelm.202400348.

18. Wali, Q.; Ar Rabbani, N.; Afrin, S.; Lee, I.E.; Khan, M.Y. Advances in electron and hole transport layers-free perovskite solar cells. *Engineering Research Express* 8 (2026) 072301. DOI: 10.1088/2631-8695/ae493c.

19. Huang, S.; Guan, B.; Li, J. Fabrication of efficient and simple-structured perovskite solar cells using a multifunctional Biocolina surface treatment. *ChemSusChem* 17 (2024) e202301873. DOI: 10.1002/cssc.202301873.

20. Deng, J.; Huang, X.; Che, Y.; et al. Salt-based catalyzer to aid heterogeneous nucleation enabling >23% efficient electron-transport-layer-free perovskite solar cells. *Advanced Functional Materials* 34 (2024) 2408392. DOI: 10.1002/adfm.202408392.

21. Yoon, J.K.; Ahn, Y.; Ryu, H.; Shin, Y.J.; Kim, W.S.; Kim, K.; Park, J.H. Spectroscopic investigation of interfacial electron extraction and recombination at azaacene-based ETLs in perovskite solar cells. *ACS Applied Optical Materials* 4 (2026) 1226–1233. DOI: 10.1021/acsaom.6c00093.

22. Mularso et al. 2D perovskite induced back surface field for efficient and stable electron-transport-layer-free perovskite solar cells. *Chemical Engineering Journal* 524 (2025) 169306. DOI: 10.1016/j.cej.2025.169306.

23. Shu et al. Organosulfide–halide perovskite heterojunction enables electron transport layer-free $CsPbI_3$ perovskite solar cells. *ACS Energy Letters* 10 (2025) 3834–3840. DOI: 10.1021/acsenergylett.5c01776.

24. Shi et al. Interface engineering for efficient ETL-free perovskite solar cells via self-assembled bifunctional monolayer. *Applied Surface Science* 684 (2024) 161950. DOI: 10.1016/j.apsusc.2024.161950.

25. Sen, R.; Yadav, M. Optimizing Cs_2TiBr_6-based PSCs with graphene quantum dots. *Engineering Proceedings* 56 (2023) 180. DOI: 10.3390/ASEC2023-15298.

26. Jubu, P. R.; Awoji, M. O.; Akeredolu, B. J.; Adepoju, A. T.; Ikwe, S. J.; Igba, D. S.; Aungwa, F.; Ikpa, T. M.; Nwachukwu, I. M.; Oguzie, E. E. High-efficiency Cs_2TiBr_6 lead-free perovskite solar cell enabled by all-inorganic CZTS/NiO double hole transport layer: A numerical simulation study. *Physics Access* 6(1) (2026). DOI: 10.47514/phyaccess.2026.6.1.004.Rühle (2016).

27. Jubu, P. R.; Abi, O. D.; Mbalaha, Z. S.; Nwokolo, I. K.; Aransiola, A. O.; Amakom, C.; Udofia, K.; Goje, A. A.; Ayogu, I. I.; Igba, D. S.; Gururani, M. M.; Oguzie, E. E. Numerical optimization of photovoltaic performance of cesium titanium bromide perovskite solar cells using dual copper oxide hole transport layers. *African Scientific Reports* 5 (2026) 488. DOI: 10.46481/asr.2026.5.2.488

28. Ruhle 2026 Rühle, S. Tabulated values of the Shockley–Queisser limit for single junction solar cells. *Solar Energy* 130 (2016) 139–147. DOI: 10.1016/j.solener.2016.02.015.

29. Rahman, M.A.; Alam, M.J. Machine learning-guided SCAPS-1D design of lead-free $CH_3NH_3SnI_3$ perovskite solar cells with 40.17% simulated PCE. *Journal of Materials Science: Materials in Engineering* 21 (2026) 62. DOI: 10.1186/s40712-026-00426-9.

30. Danladi, E.; Gyuk, P.M.; Tasie, N.N.; et al. Impact of hole transport material on perovskite solar cells with different metal electrode: A SCAPS-1D simulation insight. *Heliyon* 9 (2023) e16838. DOI: 10.1016/j.heliyon.2023.e16838.

31. Mendes, J.L.; Gao, W.; Martin, J.L.; Carl, A.D.; Deskins, N.A.; Granados-Focil, S.; Grimm, R.L. Interfacial states, energetics, and atmospheric stability of large-grain antifluorite Cs_2TiBr_6. *Journal of Physical Chemistry C* 124 (2020) 24289–24297. DOI: 10.1021/acs.jpcc.0c08719.

32. Naikaew, A.; Burimart, S.; Srathongsian, L.; Seriwattanachai, C.; Sakata, P.; Choodam, K.; Khotmungkhun, K.; Kanlayakan, W.; Pansa-Ngat, P.; Thant, K. K. S.; Kanlayapattamapong, T.; Ruankham, P.; Nakajima, H.; Supruangnet, R.; Kanjanaboos, P. Solvent-tailored carbon paste for effective carbon-based perovskite solar cells. *Solar RRL* 9(8) (2025) 2400910. DOI: 10.1002/solr.202400910

33. Danladi, E.; Oguzie, E.E.; Ezema, F.I. Highly efficient 25.562% $Cs_2AgBiBr_6$ double perovskite solar cell with copper barium tin sulfide and ZnO as charge transport channels: An intuition from a theoretical study using SCAPS-1D. *Journal of Photonics for Energy* 15 (2025) 024501. DOI: 10.1117/1.JPE.15.024501.

34. Qirong, Z.; Bao, Z.; Yongmao, H.; Liang, L.; Zhuoqi, D.; Zaixin, X.; Xiaobo, Y. A study on numerical simulation optimization of perovskite solar cell based on CuI and C_{60}. *Materials Research Express* 9 (2022) 036401. DOI: 10.1088/2053-1591/ac5a34.

35. Imani, S.; Seyed-Talebi, S.M.; Beheshtian, J.; et al. Simulation and characterization of $CH_3NH_3SnI_3$-based perovskite solar cells with different Cu-based hole transporting layers. *Applied Physics A* 129 (2023) 143. DOI: 10.1007/s00339-023-06428-0.

36. Jubu, P.R.; Otor, A.D.; Abutu, A.N.; et al. Numerical simulation of Cs_2TiBr_6-based all-inorganic photovoltaic perovskite solar cell employing SCAPS-1D software. *Journal of the Nigerian Society of Physical Sciences* 8 (2026) 3366. DOI: 10.46481/jnsps.2026.3366.

37. Jubu, P. R.; Elzawiei, Y. S. M.; Aungwa, F.; Aransiola, A. O.; Udofia, K. I.; Amakom, C.; Nwokolo, I. K.; Abi, O. D.; Gururani, M. M.; Ayogu, I. I.; Obi, I. J.; Oguzie, E. E. Interface-engineered HTL-free mixed-cation perovskite solar cells with ZnO/$BaSnO_3$ bilayer electron transport architecture: A SCAPS-1D investigation toward near-ideal photovoltaic performance. *Hybrid Advances* 14 (2026) 100721. DOI: 10.1016/j.hybadv.2026.100721.

38. Singh, P.; Ravindra, N.M. Temperature dependence of solar cell performance—an analysis. *Solar Energy Materials and Solar Cells* 101 (2012) 36. DOI: 10.1016/j.solmat.2012.02.019.

39. Lundstrom, M.S. et al. Coupled process/device modeling and point defect engineering of $Cu(In,Ga)Se_2$ solar cells. *IEEE Journal of Photovoltaics* (2024). DOI: 10.1109/JPHOTOV.2024.3366652.

40. Sakowski, K.; Strąk, P.; Kempisty, P.; et al. Coulomb contribution to Shockley–Read–Hall recombination. *Materials* 17 (2024) 4581. DOI: 10.3390/ma17184581.

41. Xiang, X.; Sommer, D.E.; Gehrke, A.; Dunham, S.T. Coupled process/device modeling and point defect engineering of $Cu(In,Ga)Se_2$ solar cells. *IEEE Journal of Photovoltaics* 14 (2024). DOI: 10.1109/JPHOTOV.2024.3366652.

42. Heredia-Rios, M. J.; Hernandez-Martinez, L.; Linares-Aranda, M.; Moreno-Moreno, M.; Méndez, J. F. Analysis of losses associated with series resistance (Rs) in simple-structured c-Si solar cells. *Energies* 17(7) (2024) 1520. DOI: 10.3390/en17071520

43. Li, H.; Huang, Y.; Zhu, M.; Yan, P.; Sheng, C. Analyzing efficiency of perovskite solar cells under high illumination intensities by SCAPS device simulation. *Nanomaterials* 15 (2025) 286. DOI: 10.3390/nano15040286.

44. Michaelson, H.B. The work function of the elements and its periodicity. *Journal of Applied Physics* 48 (1977) 4729. DOI: 10.1063/1.323539.

45. Siddique, M.A.B.; Parves, M.S.; Tarekuzzaman, M.; et al. Exploring optoelectronic behavior and solar cell efficiency of double halide perovskites M_2KIrCl_6 (M = Cs, Rb) through DFT and SCAPS-1D. *Langmuir* 41 (2025) 19797. DOI: 10.1021/acs.langmuir.5c01639.

46. Kumar, M.; Rani, S.; Wang, X.; Singh, V.N. Unlocking the full potential of solar cell materials: Parameter sensitivity analysis and optimization using response surface modeling. *Materials Advances* 6 (2025) 1–10. DOI: 10.1039/D4MA00728J.

47. Jakhrani, A.Q.; Othman, A.-K.; Rigit, A.R.H.; Samo, S.R.; Kamboh, S.A. Sensitivity analysis of a standalone photovoltaic system model parameters. *Journal of Applied Sciences* 13 (2013) 220–231. DOI: 10.3923/jas.2013.220.231.

48. Sandberg, O.J.; Kumar, M.; Stolterfoht, M.; Neher, D.; Armin, A. Analytical model for interface-recombination-limited ideality factors in p-i-n perovskite solar cells. *APL Energy* 3 (2025) 036107. DOI: 10.1063/5.0286898.

49. Zheng, Y.; Li, Y.; Xue, R.; et al. Towards 26% efficiency in inverted perovskite solar cells via interfacial flipped band bending and suppressed deep-level traps. *Energy & Environmental Science* 17 (2024) 1153–1162. DOI: 10.1039/D3EE03435F.

50. Shi, Z.; Wang, Y.; Wang, Y.; et al. Room-temperature crystallized phase-pure α-$FAPbI_3$ perovskite with in-situ grain-boundary passivation. *Advanced Science* 11 (2024) 2400275. DOI: 10.1002/advs.202400275.

51. Zhao, K.; Yao, L.; Değer, C.; et al. Mitigating residual MA^+ for stable $FAPbI_3$ perovskite photovoltaics. *Nature Communications* 16 (2025) 10074. DOI: 10.1038/s41467-025-65045-y.

52. Trejo-Zamudio, D.; Morales-Luna, M.; Aruna-Devi, R.; et al. Optoelectronic properties of $CuSbS_2$ and $Cu_{12}Sb_4S_{13}$ thin films for thermoelectric applications. *Materials Research* 26 (2023) e20220469. DOI: 10.1590/1980-5373-MR-2022-0469.

53. Bella, M.; Rivero, C.; Blayac, S.; Basti, H.; Record, M.C.; Boulet, P. Oleylamine-assisted solvothermal synthesis of copper antimony sulfide nanocrystals: Morphology and phase control. *Materials Research Bulletin* 90 (2017) 188–194. Note: the DOI in the supplied typeset file is incomplete and should be checked before submission.

54. Xue, R.; Gao, G.; Yang, L.; Xu, L.; Zhang, Y.; Zhu, J. The impact of thickness-related grain boundary migration on hole concentration and mobility of p-type transparent conducting CuI films. *RSC Advances* 14 (2024) 9072–9079. DOI: 10.1039/D4RA00704B.

55. Jun, T.; Kim, J.; Sasase, M.; Hosono, H. Material design of p-type transparent amorphous semiconductor, Cu–Sn–I. *Advanced Materials* 30 (2018) 1706573. DOI: 10.1002/adma.201706573.

56. Hao, M.; Duan, T.; Ma, Z.; et al. Flattening grain-boundary grooves for perovskite solar cells with high optomechanical reliability. *Advanced Materials* 35 (2023) 2211155. DOI: 10.1002/adma.202211155.

57. Yang, J.; Tang, W.; Yuan, R.; et al. Defect mitigation using D-penicillamine for efficient methylammonium-free perovskite solar cells with high operational stability. *Chemical Science* 12 (2021) 2050–2059. DOI: 10.1039/D0SC06354A.

58. Song, Y.; Li, L.; Bi, W.; et al. Atomistic surface passivation of $CH_3NH_3PbI_3$ perovskite single crystals for highly sensitive coplanar-structure X-ray detectors. *Research* 2020 (2020) 5958243. DOI: 10.34133/2020/5958243.

59. Levine, I.; Al-Ashouri, A.; Musiienko, A.; et al. Charge transfer rates and electron trapping at buried interfaces of perovskite solar cells. *Joule* 5 (2021) 2915–2933. DOI: 10.1016/j.joule.2021.07.016.

60. Wang, H.; Yu, Z.; Jiang, X.; Li, J.; Cai, B.; Yang, X.; Sun, L. Efficient and stable inverted planar perovskite solar cells employing CuI as hole-transporting layer prepared by solid-gas transformation. *Energy Technology* 5 (2017) 1836–1843. DOI: 10.1002/ente.201700422.

61. Srivastava, R.P.; Jung, H.-S.; Khang, D.-Y. Transfer-printed cuprous iodide (CuI) hole transporting layer for low-temperature processed perovskite solar cells. *Nanomaterials* 12 (2022) 1467. DOI: 10.3390/nano12091467.

62. Galagan, Y.; Shanmugam, S.; Teunissen, J.P.; et al. Solution processing of back electrodes for organic solar cells with inverted architecture. *Solar Energy Materials and Solar Cells* 130 (2014) 163–169. DOI: 10.1016/j.solmat.2014.07.007.

63. Giuri, A.; Rolston, N.; Colella, S.; et al. Robust, high-performing maize–perovskite-based solar cells with improved stability. *ACS Applied Energy Materials* 4 (2021) 11194–11203. DOI: 10.1021/acsaem.1c02058.

64. Kawano, Y.; Chantana, J.; Nishimura, T.; Mavlonov, A.; Minemoto, T. Manipulation of [Ga]/([Ga] + [In]) profile in 1.4-μm-thick $Cu(In,Ga)Se_2$ thin film on flexible stainless-steel substrate for enhancing short-circuit current density and conversion efficiency. *Solar Energy* 204 (2020) 231–237. DOI: 10.1016/j.solener.2020.04.069.

65. Chen, W.; Liu, F.-Z.; Feng, X.-Y.; Djurišić, A.B.; Chan, W.K.; He, Z.-B. Cesium-doped NiO_x as an efficient hole extraction layer for inverted planar perovskite solar cells. *Advanced Energy Materials* 7 (2017) 1700722. DOI: 10.1002/aenm.201700722.

66. Gao, X.-K.; Li, C.-C.; Lai, Y.-H.; et al. Cesium iodide incorporation enables high-efficiency and thermally stable inverted perovskite solar cells with low-temperature NiO_x. *ACS Applied Energy Materials* 8 (2025) 14576–14583. DOI: 10.1021/acsaem.5c02241.

67. Qin, W.; Ali, W.; Wang, J.; et al. Suppressing non-radiative recombination in metal halide perovskite solar cells by synergistic effect of ferroelasticity. *Nature Communications* 14 (2023) 256. DOI: 10.1038/s41467-023-35837-1.

68. Han, Q.; Ding, J.; Bai, Y.; et al. Carrier dynamics engineering for high-performance electron-transport-layer-free perovskite photovoltaics. *Chem* 4 (2018) 2405–2417. DOI: 10.1016/j.chempr.2018.08.004.

69. Lin, X.; Jumabekov, A.N.; Lal, N.N.; et al. Dipole-field-assisted charge extraction in metal-perovskite-metal back-contact solar cells. *Nature Communications* 8 (2017) 613. DOI: 10.1038/s41467-017-00588-3.

70. Li, M.; Park, S.Y.; Wang, J.; et al. Nickel-doped graphite and fusible alloy bilayer back electrode for vacuum-free perovskite solar cells. *ACS Energy Letters* 8 (2023) 2940–2945. DOI: 10.1021/acsenergylett.3c00852.

71. Domanski, K.; Correa-Baena, J.-P.; Mine, N.; et al. Not all that glitters is gold: Metal-migration-induced degradation in perovskite solar cells. *ACS Nano* 10 (2016) 6306–6314. DOI: 10.1021/acsnano.6b02613.

72. Parvazian, E.; Beynon, D.; Jenkins, O.; et al. Selecting non-halogenated low-toxic hole transporting materials for roll-to-roll perovskite solar cells using carbon electrodes. *Communications Materials* 5 (2024) 82. DOI: 10.1038/s43246-024-00516-1.

73. Lin, Z.; Xiong, Z.; Guo, H.; et al. Research progress on perovskite solar cells based on organic carbon electrodes. *Carbon Letters* 35 (2025) 1833–1860. DOI: 10.1007/s42823-025-00935-1.

74. Bidikoudi, M.; Stathatos, E. Chalcogenides in perovskite solar cells with a carbon electrode: State of the art and future prospects. *Nanomaterials* 14 (2024) 1783. DOI: 10.3390/nano14221783.

75. Reza, M.S.; Ghosh, A.; Reza, M.S.; Aktarujjaman, M.; Talukder, M.J.; Aljazzar, S.O.; Al-Humaidi, J.Y.; Mukhrish, Y.E. Enhancing the performance of Cs_2TiBr_6 lead-free perovskite solar cells: A simulation study on the impact of electron and hole transport layers. *Langmuir* 41 (2025) 6987–7007. DOI: 10.1021/acs.langmuir.4c05265.

76. Tahir, S.; Ashfaq, A.; Mushtaq, S.; et al. Performance optimization of inorganic Cs_2TiBr_6 based perovskite solar cell via numerical simulation. *Energy Technology* 11 (2023) 2300359. DOI: 10.1002/ente.202300359.

77. Shivesh, K.; Alam, I.; Kushwaha, A.K.; Kumar, M.; Singh, S.V. Investigating the theoretical performance of Cs_2TiBr_6-based perovskite solar cell with La-doped $BaSnO_3$ and $CuSbS_2$ as the charge transport layers. *International Journal of Energy Research* 46 (2022) 6045–6064. DOI: 10.1002/er.7546.

78. Kaur, J.; Sharma, A.K.; Basu, R. Numerical simulation and performance optimization of non-toxic Cs_2TiBr_6 single-halide perovskite solar cell by introducing interfacial defect layers. *Optical and Quantum Electronics* 57 (2025) 152. DOI: 10.1007/s11082-024-08023-w.

79. Jacobsson, T.J.; Tress, W.; Correa-Baena, J.-P.; Edvinsson, T.; Hagfeldt, A. Room temperature as a Goldilocks environment for $CH_3NH_3PbI_3$ perovskite solar cells: The importance of temperature on device performance. *Journal of Physical Chemistry C* 120 (2016) 11382–11393. DOI: 10.1021/acs.jpcc.6b02858.

80. Wan, Z.; Wei, R.; Zhao, H.; et al. Thermal management technologies for improving the thermal stability of perovskite solar cells. *Nano-Micro Letters* 18 (2026) 207. DOI: 10.1007/s40820-025-02047-x.

81. Yilmaz, C.; Buyruk, A.; Shi, Y.; et al. Perovskite solar cells with enhanced thermal fatigue resistance under extreme temperature cycling. *Nature Communications* 17 (2026) 3669. DOI: 10.1038/s41467-026-70293-7.

82. Varshni, Y.P. Temperature dependence of the energy gap in semiconductors. *Physica* 34 (1967) 149–154. DOI: 10.1016/0031-8914(67)90062-6.

83. Caprioglio, P.; Stolterfoht, M.; Wolff, C.M.; Unold, T.; Rech, B.; Albrecht, S.; Neher, D. On the relation between the open-circuit voltage and quasi-Fermi level splitting in efficient perovskite solar cells. *Advanced Energy Materials* 9 (2019) 1901631. DOI: 10.1002/aenm.201901631.

84. Wang, Z.; Lin, Q.; Wenger, B.; et al. High irradiance performance of metal halide perovskites for concentrator photovoltaics. *Nature Energy* 3 (2018) 855–861. DOI: 10.1038/s41560-018-0220-2.

85. Jones, M.D.K.; Dawson, J.A.; Campbell, S.; Barrioz, V.; Whalley, L.D.; Qu, Y. Modelling interfaces in thin-film photovoltaic devices. *Frontiers in Chemistry* 10 (2022) 920676. DOI: 10.3389/fchem.2022.920676.

86. Eames, C.; Frost, J.M.; Barnes, P.R.F.; O'Regan, B.C.; Walsh, A.; Islam, M.S. Ionic transport in hybrid lead iodide perovskite solar cells. *Nature Communications* 6 (2015) 7497. DOI: 10.1038/ncomms8497.

87. Meloni, S.; Moehl, T.; Tress, W.; et al. Ionic polarization-induced current–voltage hysteresis in $CH_3NH_3PbX_3$ perovskite solar cells. *Nature Communications* 7 (2016) 10334. DOI: 10.1038/ncomms10334.

88. Zhu, S.; Tian, J.; Zhang, J.; Zhang, J.; Liu, X. Improving the interfacial contact of screen-printed carbon electrodes for perovskite solar cells. *ACS Applied Energy Materials* 4 (2021) 5554–5559. DOI: 10.1021/acsaem.1c00232.

89. Beynon, D.; Parvazian, E.; Hooper, K.; et al. All-printed roll-to-roll perovskite photovoltaics enabled by solution-processed carbon electrode. *Advanced Materials* 35 (2023) e2208561. DOI: 10.1002/adma.202208561.

90. Su, H.; Xiao, J.; Li, Q.; Peng, C.; Zhang, X.; Mao, C.; Yao, Q.; Lu, Y.; Ku, Z.; Zhong, J.; Li, W.; Peng, Y.; Huang, F.; Cheng, Y.-B. Carbon film electrode based square-centimeter scale planar perovskite solar cells exceeding 17% efficiency. *Materials Science in Semiconductor Processing* 107 (2020) 104809. DOI: 10.1016/j.mssp.2019.104809.